https://doi.org/10.5194/wes-2023-133
Preprint. Discussion started: 6 November 2023

eawe european academy of wind energy
Open Access WIND ENERGY SCIENCE DISCUSSIONS

On the power and control of a misaligned rotor – Beyond the cosine law –

Simone Tamaro, Filippo Campagnolo, and Carlo L. Bottasso
Wind Energy Institute, Technical University of Munich, 85748 Garching b. München, Germany
Correspondence: Carlo L. Bottasso (carlo.bottasso@tum.de)

Abstract.

We present a new model to estimate the performance of a wind turbine operating in misaligned conditions. The model is based on the classic momentum and lifting-line theories, considering a misaligned rotor as a lifting wing of finite span, and accounts for the combined effects of both yaw and uptilt angles.

Improving on the classical empirical cosine law in widespread use, the new model reveals the dependency of power not only on the misalignment angle, but also on some rotor design parameters and – crucially – on the way a rotor is governed when it is yawed out of the wind. Additionally, the model also shows that a sheared inflow is responsible for the observed lack of symmetry for positive and negative misalignment angles. Notwithstanding its simplicity and insignificant computational cost, the new proposed approach is in excellent agreement with large eddy simulations (LES) and wind tunnel experiments.

Building on the new model, we derive the optimal control strategy for maximizing power on a misaligned rotor. Additionally, we maximize the total power of a cluster of two turbines by wake steering, improving on the solution based on the cosine law.

1 Introduction

Wind farm control by wake steering consists of deflecting the wake away from downstream rotors to boost the total power of a plant (Meyers et al., 2022). The effectiveness of this control strategy has been proven numerically (Jiménez et al., 2010), experimentally in the wind tunnel (Campagnolo et al., 2016), as well as in field tests (Fleming et al., 2019; Doekemeijer et al., 2021). At the core of the power-boosting ability of wake steering is a trade-off: on the one hand, there is an enhanced momentum of the inflow at a downstream turbine when a wake is shifted laterally away from it; on the other hand, some power is lost at the upstream misaligned rotor, because it does not point into the wind anymore. In general the trade-off budget is positive, in the sense that the power that is gained downstream is larger than the one lost upstream. The problem is however highly complex: downstream, power capture is determined by the interaction of the impinged rotor with the wake that, in turn, is influenced by the ambient conditions and those of the wake-shedding turbine; upstream, power losses depend on the inflow characteristics, but also on the rotor and on the way it is governed. Understanding and controlling this delicate balance between upstream and downstream behavior is clearly of paramount importance for improving the power capture of wind farms by wake steering. Great progress has been made in recent years to understand, model and control wakes (see for example the review in Meyers et al. (2022)), i.e. on the "downstream" aspect of the problem. However, the "upstream" aspect remains much

https://doi.org/10.5194/wes-2023-133
Preprint. Discussion started: 6 November 2023

eawe european academy of wind energy
Open Access WIND ENERGY SCIENCE DISCUSSIONS

less explored and understood. How much power does a yawed turbine really lose? And what inflow, rotor and rotor-control parameters influence its behavior? It is a major ambition of this paper to try and answer these questions.

The aerodynamic power P of a wind turbine is customarily written as $P = 1/2\rho A u_\infty^3 C_P$, where ρ is the air density, A the rotor swept area, u_∞ the ambient wind speed, and C_P the power coefficient. When a turbine is misaligned with respect to the wind vector by an angle γ, the rotor-orthogonal velocity component becomes $u_\infty \cos\gamma$. Accordingly, one would expect the yaw-induced power loss to be $\eta_P = P/P_0 = \cos^3\gamma$, where P_0 is the aerodynamic power produced for $\gamma = 0$. Unfortunately, this is only a naive interpretation of the true behavior of a misaligned rotor, and its predictions are not confirmed by experimental and numerical observations (Liew et al., 2020). To reflect this fact, a pragmatic solution has been adopted by most of the literature, where power losses due to misalignment are assumed to obey the simple law $\eta_P \approx \cos^{p_p}\gamma$, where p_p is a tunable parameter.

Unsurprisingly, since such a model is not based on actual physics, a large spread of values for p_p has been reported in the literature. In wind tunnel experiments with scaled models, Campagnolo et al. (2020a) measured $p_p = 2.1$, Krogstad and Adaramola (2012) and Bartl et al. (2018) reported $p_p \approx 3$, whereas Medici (2005) found a value $p_p = 2$. Numerically, Fleming et al. (2015) measured $p_p = 1.88$ on the NREL 5 MW wind turbine (Jonkman et al., 2009), whereas Draper et al. (2018) obtained values between 1.3 and 2.5 for scaled wind turbine models operating in waked inflow conditions. The power production in misaligned conditions has also been measured in multiple field tests. For example, Fleming et al. (2017) reported a value of 1.41 for an Envision 4 MW turbine; Dahlberg and Montgomerie (2005) published a range of values for p_p between 1.9 and 5.1 at an offshore plant. More recently, Hulsman et al. (2022) observed $2 < p_p < 2.5$ at an onshore wind farm in the north of Germany.

The high scatter characterizing the p_p coefficients reported in the literature is a relevant source of uncertainty, creating a significant hindrance to the development of power-boosting wind farm control strategies.

The large scatter in the cosine exponent suggests that some relevant phenomena are not captured by the $\cos^{p_p}$ law. In hindsight, this is to be expected, because this simple model fails to explicitly represent how the power coefficient C_P changes when a turbine is misaligned, and somehow absorbs this effect into the tunable exponent. Some indications that there is more to this problem than a simple power cosine law have already been reported by various authors. Based on experiments and numerical simulations, Campagnolo et al. (2023), Cossu (2021a, b) and Heck et al. (2022) suggested that the power of a misaligned rotor strongly depends on its loading, in the form of the thrust coefficient C_T (which, clearly, has also a strong effect on the behavior of the wake (Cossu, 2021a, b). Other variables that have been shown to play a role on power losses are related to the inflow. Recently, Draper et al. (2018) and Liew et al. (2020) have observed that power losses in misaligned conditions differ depending on whether a rotor is waked or not. Howland et al. (2020) observed a significant influence of shear and veer, while Simley et al. (2021) measured a strong dependency on inflow speed. The behavior of power losses has also been shown to depend on the direction of yaw misalignment, and not only on its magnitude as implied by the power cosine law. This asymmetric behavior of yaw misalignment has been observed by Fleming et al. (2015); Schottler et al. (2017); Fleming et al. (2018); Campagnolo et al. (2020a), among others. However, an agreement on which misalignment direction yields more or less power has not been reached yet.

https://doi.org/10.5194/wes-2023-133
Preprint. Discussion started: 6 November 2023

eawe european academy of wind energy
Open Access WIND ENERGY SCIENCE DISCUSSIONS

In this paper, we present a new analytical model for misaligned wind turbine rotors. The proposed approach combines the classic momentum and lifting-line theories, considering a misaligned rotor as a lifting wing of finite span, in close parallel to the analysis conducted for helicopter rotors in forward flight (Johnson, 1995). Very recently, Heck et al. (2022) published a misaligned rotor model based on similar arguments, although their approach does not explain the lack of symmetry with respect to yaw direction. The present model includes the effects of wind shear, which is shown to be the culprit for the observed break of symmetry with respect to the misalignment direction. For improved accuracy, the model also includes the effects of the uptilt angle, as it contributes to the overall misalignment of the rotor with respect to the wind vector. The resulting equations are integrated over the blade span and averaged over one rotor revolution, leading to a semi-analytical formulation of negligible computational cost that can be readily coupled with engineering wake models such as FLORIS (NREL, 2023b) or PyWake (Pedersen et al., 2019). However, the model governing equations could also be integrated numerically and embedded into blade element momentum (BEM) codes (Hansen, 2015), such as the AeroDyn package (NREL, 2023a) implemented in OpenFAST (NREL, 2023c).

The proposed semi-analytical model shows that the behavior of a misaligned rotor does not follow the $\cos^{p_p}$ law, contradicting this empirical formula in widespread use. Additionally, the new model clarifies the behavior of power capture with respect to some rotor design parameters and – even more importantly – with respect to the way a rotor is governed when it is misaligned. This is an effect that has been neglected in all analyses conducted so far, and that most probably explains the large scatter observed by various authors. Building on these results, we derive the optimal strategy for maximizing power capture when pointing a rotor away from the wind. Finally, we implement the semi-analytical model in FLORIS and we optimize the power of a cluster of two turbines. We obtain setpoints that differ from those that can be computed with the empirical $\cos^{p_p}$ law, and that lead to a slight improvement of the cluster power.

The new models exhibits an excellent match with high-fidelity LES simulations obtained with a TUM-modified version of NREL's large eddy simulator actuator line model (LES-ALM) SOWFA (Fleming et al., 2014; Wang et al., 2019, 2018). Additionally, the model is further validated with wind tunnel data from experiments conducted with the TUM G1 scaled wind turbines (Bottasso and Campagnolo, 2022a; Campagnolo et al., 2020b).

The paper is organized as follows: Sect. 2 presents the new formulation and Sect. 3 its validation with respect to simulated and experimental data, while Sect. 4 analyzes the effects of the new model on wake steering. Finally, Sect. 5 draws conclusions and offers an outlook towards future work.

2 Misalignment model

2.1 Frames of reference

Three reference frames are necessary to completely characterize a misaligned rotor interacting with the wind, as shown in Fig. 1: a *ground-fixed* reference frame and a *nacelle-fixed* reference frame, which together describe the relative orientation of the rotor with respect to the ground, and a *wake-deflection intrinsic frame*, which describes the relative orientation of the rotor with respect to the incoming wind vector.

https://doi.org/10.5194/wes-2023-133
Preprint. Discussion started: 6 November 2023

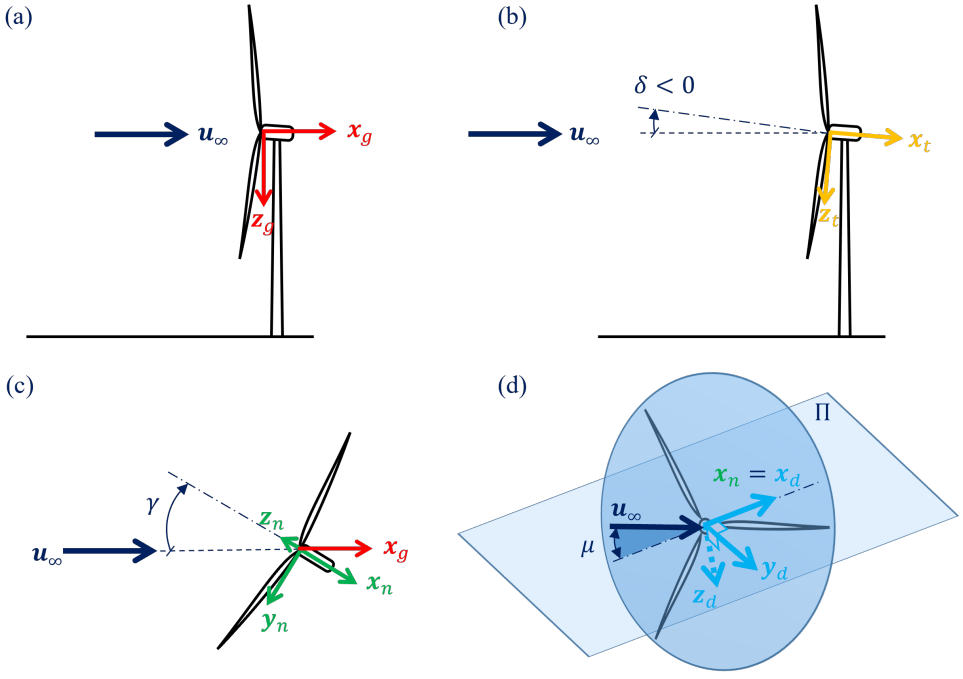

Figure 1. Reference frames used in the derivation of the model. Ground-fixed wind-aligned reference frame (in red, subscript g) **(a)**; intermediate frame, obtained by the tilt rotation δ about the horizontal axis $\boldsymbol{y}_g$ (in orange, subscript t) **(b)**; nacelle-fixed reference frame, obtained from t by a yaw rotation γ about the vertical axis $\boldsymbol{z}_g$ (in green, subscript n) **(c)**; plane Π formed by the wind vector $\boldsymbol{u}_\infty$ and the rotor axis $\boldsymbol{x}_n$; the plane contains the $\boldsymbol{x}_d$ and $\boldsymbol{y}_d$ unit vectors of the wake-deflection intrinsic frame (in light blue, subscript d) **(d)**. Rotations are positive according to the right hand rule; notice that the value of the uptilt angle of the rotor in panel **(b)** is therefore negative.

The ground-fixed wind-aligned frame of reference is indicated with a subscript g and is defined by the right-handed triad of unit vectors $\mathcal{F}_g = \{\boldsymbol{x}_g, \boldsymbol{y}_g, \boldsymbol{z}_g\}$. $\boldsymbol{z}_g$ points vertically down towards the ground, $\boldsymbol{x}_g$ is parallel to the terrain pointing downstream and is contained in the plane formed by the wind vector $\boldsymbol{u}_\infty$ and $\boldsymbol{z}_g$; finally, $\boldsymbol{y}_g$ completes a right-handed triad. In the following, for simplicity we consider the wind vector to be parallel to the terrain, i.e. $\boldsymbol{u}_\infty \parallel \boldsymbol{x}_g$, although this is not strictly necessary.

The nacelle-fixed frame of reference is indicated with a subscript n and is defined by the triad of unit vectors $\mathcal{F}_n = \{\boldsymbol{x}_n, \boldsymbol{y}_n, \boldsymbol{z}_n\}$. $\mathcal{F}_n$ is obtained from $\mathcal{F}_g$ by two successive rotations: a first rotation by the *tilt* angle δ about the horizontal axis $\boldsymbol{y}_g$, followed by a second rotation by the *yaw* angle γ about the vertical axis $\boldsymbol{z}_g$. Both rotations are positive about their respective axes according to the right hand rule (notice that, according to this definition, the typical uptilt of an upwind turbine results in a negative value for δ).

However, the interaction of the rotor with the flow depends only on their mutual orientation, and not on how they are oriented with respect to the ground, which is a fundamental principle of fluid mechanics known as Galilean relativity. Therefore, a third frame is necessary, which is termed here *wake-deflection intrinsic frame* and is indicated with a subscript d. The frame is formed

https://doi.org/10.5194/wes-2023-133
Preprint. Discussion started: 6 November 2023

eawe european academy of wind energy
Open Access WIND ENERGY SCIENCE DISCUSSIONS

by a right-handed triad of unit vectors $\mathcal{F}_d = \{\boldsymbol{x}_d, \boldsymbol{y}_d, \boldsymbol{z}_d\}$. Vector $\boldsymbol{x}_d$ is parallel to the rotor axis, i.e. $\boldsymbol{x}_d = \boldsymbol{x}_n$. Together, the rotor axis $\boldsymbol{x}_d$ and the wind velocity vector $\boldsymbol{u}_\infty$ define the Π plane. The angle in the Π plane between these two vectors is the *true misalignment angle* μ:

$$\cos\mu = \frac{\boldsymbol{u}_\infty}{u_\infty} \cdot \boldsymbol{x}_n, \tag{1}$$

where $u_\infty = |\boldsymbol{u}_\infty|$ is the scalar wind speed. The unit vector $\boldsymbol{z}_d$ is orthogonal to the Π plane, i.e. $\boldsymbol{z}_d = \boldsymbol{x}_d \times \boldsymbol{u}_\infty / (u_\infty \sin\mu)$, while unit vector $\boldsymbol{y}_d$ is finally chosen to form a right-handed triad. Using the coordinate transformations in Appendix A, it can be readily shown that $\cos\mu = \cos\delta\cos\gamma$, i.e. the total misalignment is caused by both the tilt and yaw angles, the former typically being neglected in most wake models. Notice that, given its definition, the misalignment angle μ is always positive, because $\boldsymbol{z}_d$ flips from one side of the Π plane to the other, depending on the relative orientation of the wind velocity and rotor axis vectors. When the wind comes from the right looking upstream in the Π plane, $\boldsymbol{z}_d$ points downwards (see Fig. 1d), whereas it points upwards when the wind comes from the left.

Figure 2 shows a visualization of the wakes developing behind a wind turbine rotor for two different pairs of tilt and yaw values: $\delta = 0°, \gamma = -30°$; and $\delta = -28.43°, \gamma - 10°$. Both pairs correspond to a same true misalignment $\mu = -30°$. The figure confirms that the wake is invariant for an observer on the $\mathcal{F}_d$ frame. This is particularly evident in the images of the longitudinal speed on the Π plane (marked with a black solid border), which are clearly identical in the two cases.

Because of what noted above, in the following the wake analysis is developed in the Π plane, instead of the horizontal one as customarily done. Transformation matrices that map vector components from one frame to the other are reported in Appendix A.

2.2 Sheared inflow

Considering a linear vertical shear of the inflow, the ambient wind speed writes

$$u_\infty(z_g) = u_{\infty,\text{hub}} \left(1 - k\frac{z_g}{R}\right). \tag{2}$$

Here $u_{\infty,\text{hub}}$ is the ambient wind speed at hub height, k is the vertical linear shear coefficient, and z_g is the vertical coordinate in the ground frame of reference, centered at the hub. By applying the coordinate transformation of Appendix A, the ambient wind speed of Eq. (2) can be written in terms of the radial r and azimuthal ψ coordinates on the rotor plane, yielding

$$u_\infty(r,\psi,\delta,\gamma) = u_{\infty,\text{hub}} \left(1 - k\frac{r}{R}\frac{\cos\delta}{\sin\mu}\left(\sin\gamma\cos\psi - \cos\gamma\sin\delta\sin\psi\right)\right). \tag{3}$$

Here ψ is positive about $\boldsymbol{x}_d$ according to the right hand rule (i.e. clockwise looking downstream), and it is measured starting from the $\boldsymbol{z}_d$ unit vector (which flips from one side of the Π plane to other depending on whether the wind blows from the right or left looking upstream, as explained in Sect. 2.1).

https://doi.org/10.5194/wes-2023-133
Preprint. Discussion started: 6 November 2023

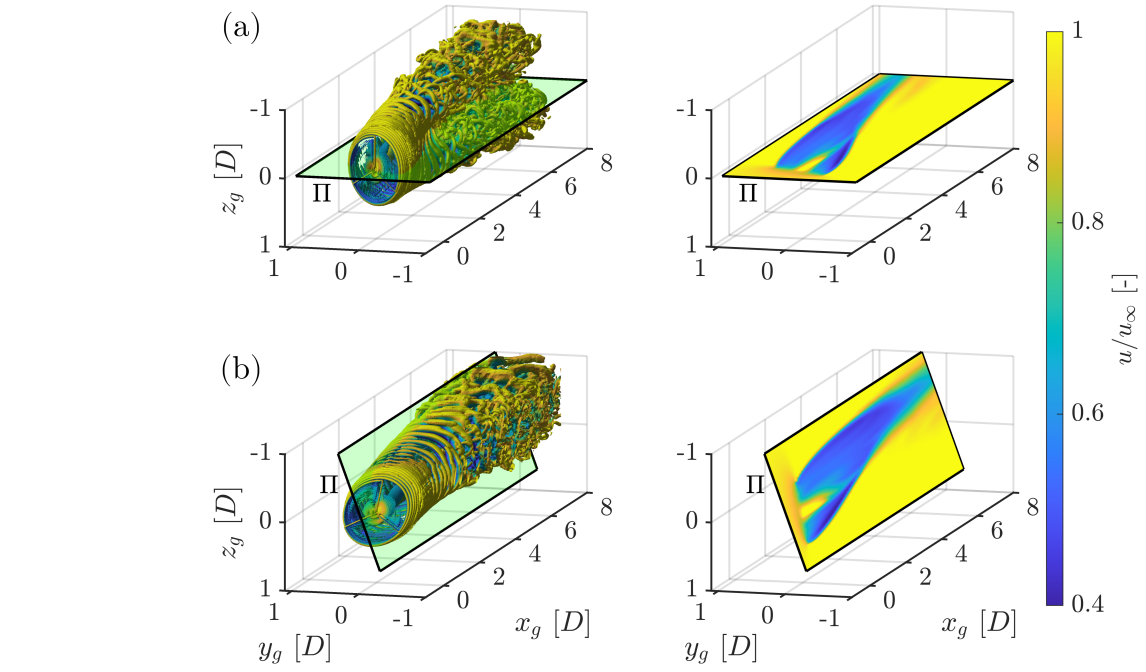

Figure 2. Visualization of the wakes developing behind a wind turbine operating in steady inflow conditions for different pairs of tilt and yaw values, all corresponding to a same total (true) misalignment $\mu = -30°$. The deflection of the wake occurs in the Π plane, marked with a black border. Top row **(a)**: $\delta = 0°$, $\gamma = -30°$; bottom row **(b)**: $\delta = -28.43°$, $\gamma = -10°$. Left column: iso surfaces of Q-criterion; right column: image of the longitudinal flow speed u/u_∞ on the Π plane. Distances are expressed in rotor diameters D. Interactive 3D versions of the figures are available at the following links: https://tinyurl.com/btcl-fig2-a **(a)**; https://tinyurl.com/btcl-fig2-b **(b)**.

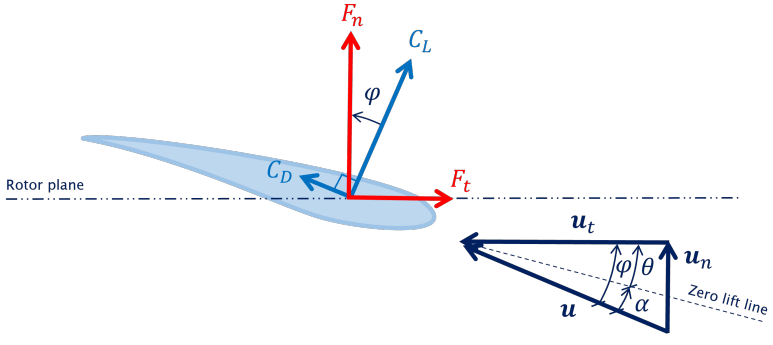

Figure 3. Blade cross section, with triangle of velocities (in blue), lift and drag (in light blue), and resulting aerodynamic force components (in red).

https://doi.org/10.5194/wes-2023-133
Preprint. Discussion started: 6 November 2023

eawe european academy of wind energy
Open Access WIND ENERGY SCIENCE DISCUSSIONS

2.3 Force and velocity components at a blade section

With reference to Fig. 3, the tangential F_t and normal F_n components of the aerodynamic force at a blade section are

$$F_t = \frac{1}{2}\rho u^2 c \left(C_L \sin\varphi - C_D \cos\varphi\right), \tag{4a}$$

$$F_n = \frac{1}{2}\rho u^2 c \left(C_L \cos\varphi + C_D \sin\varphi\right), \tag{4b}$$

where $\varphi = \tan^{-1} u_n/u_t$ is the inflow angle, $u = \sqrt{u_t^2 + u_n^2}$ is the total flow speed at the blade section, c is the sectional chord length, and finally C_L and C_D are the lift and drag coefficients, respectively. Using the coordinate transformations of Appendix A, the tangential u_t and normal u_n velocity components write

$$u_t = \Omega r + u_\infty \sin\mu \cos\psi, \tag{5a}$$

$$u_n = u_\infty \cos\mu (1 - a), \tag{5b}$$

where Ω is the angular speed of the rotor and a is the axial induction factor, which expresses how much the rotor-orthogonal component of the free-stream speed u_∞ is slowed down at the rotor disk.

2.4 Induction model

It is well known that a non-uniform description of the induction is necessary in order to accurately capture the azimuthal variation of loads on a rotor operating in non-axial conditions (Johnson, 1995). However, it appears that this is not necessary when computing integral rotor quantities such as power, torque and thrust, as in the present case. To show this, the induction is modeled here with an expansion limited to one-per-revolution (1P) harmonics, i.e.

$$a = a_0 \left(1 + \kappa_{1s} \frac{r}{R} \sin\psi + k_{1c} \frac{r}{R} \cos\psi_g\right), \tag{6}$$

where a_0 is the constant-over-the-rotor (0P) induction, r is the blade spanwise coordinate, and R is the rotor radius.

Following the classical approach used for helicopter rotors in forward flight, the sine term accounts for the tilting of the induction plane caused by the misalignment μ of the rotor with the incoming wind. As such, it is written in terms of ψ, which is measured starting from the $\boldsymbol{z}_d$ unit vector, and therefore it expresses a rotation of the induction plane about the axis normal to the wake-deflection intrinsic frame Π. The coefficient κ_{1s} can be modeled according to Coleman et al. (1945) and Pitt and Peters (1981), resulting in the expression

$$\kappa_{1s} = -\frac{15\pi}{32} \tan\left(\frac{\chi}{2}\right), \tag{7}$$

where the initial wake skew angle is $\chi = \mu + \sin\mu C_T/2$ (Jiménez et al., 2010), and $C_T = 2T/(\rho A u_{\infty,\text{hub}}^2)$ is the thrust coefficient. Notice that the definition of the skew angle differs from the one given by Eq. (20) of Jiménez et al. (2010), because of the different definition of the thrust coefficient used in that publication.

The cosine term is introduced to account for the effects on the induction caused by vertical shear. As such, it is written as a function of the azimuthal angle ψ_g, which is measured from the (vertical) $\boldsymbol{z}_g$ unit vector, and therefore it expresses a rotation

https://doi.org/10.5194/wes-2023-133
Preprint. Discussion started: 6 November 2023

eawe european academy of wind energy
Open Access WIND ENERGY SCIENCE DISCUSSIONS

of the induction plane about the (horizontal) unit vector $\boldsymbol{y}_g$. Using Eq. (A4b), it is readily found that $\psi_g = \psi \cos\mu$. Following Forsting et al. (2018), the cosine term is proportional to both the shear k and the thrust C_T coefficients, i.e.

$$\kappa_{1c} = \kappa^*_{1c} k C_T. \tag{8}$$

The sine term significantly complicates the analytical derivations of power, torque and thrust, which must now be expressed in terms of Bessel functions (Abramowitz et al., 1988) because of the term $\cos(\psi \cos\mu)$. Before attempting the modeling of the proportionality coefficient κ^*_{1c}, this term was numerically optimized to best fit the numerical simulations and experimental measurements, as explained later in Sect. 2.9.

The inclusion of the sine and cosine induction terms has only an extremely modest effect on the quality of the results. In fact the match of C_P improves by 0.35% when the sine term is included, and by 0.60% when both terms are used. Because of their modest effects, these terms are dropped from the following discussion, to simplify the resulting expressions, and they were not used in the results reported later in this article. However, these terms are retained in the software implementation of the model (Tamaro et al., 2023), and can be switched on if desired by the user.

2.5 Streamtube model

An expression for the axial induction can be derived using the concept of a streamtube (Hansen, 2015), as shown in Fig. 4 with reference to the present case of a misaligned rotor. Four stations are considered along the stream tube: inlet i; outlet o; section r^- located immediately in front of the rotor; section r^+ located immediately behind the rotor.

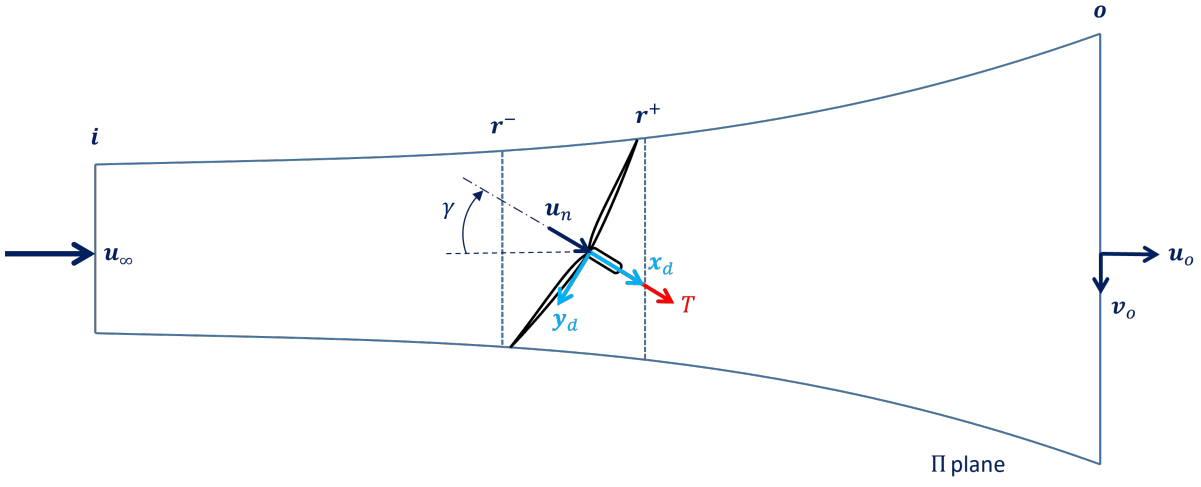

Figure 4. Schematic view of a streamtube around a misaligned wind turbine. Cross-sectional stations: inlet i, outlet o, r^- immediately in front of the rotor; r^+ immediately behind the rotor.

https://doi.org/10.5194/wes-2023-133
Preprint. Discussion started: 6 November 2023

eawe european academy of wind energy
Open Access WIND ENERGY SCIENCE DISCUSSIONS

The principle of impulse and momentum applied to the streamtube is written as

$$T\cos\mu = \dot{m}(u_\infty - u_o), \tag{9}$$

where T is the thrust force, u_o is the longitudinal flow speed at the streamtube outlet, while $\dot{m}$ is the mass flux

$$\dot{m} = \rho A u_n. \tag{10}$$

By using the thrust coefficient, Eq. (9) yields the non-dimensional longitudinal flow speed at the streamtube outlet:

$$\frac{u_o}{u_{\infty,\text{hub}}} = 1 - \frac{1}{2}\frac{C_T}{1-a_0}. \tag{11}$$

Next, Bernoulli's energy conservation theorem is applied between the streamtube inlet and the section immediately upstream of the rotor (stations i and r^- in Fig. 4), and between the section immediately downstream of the rotor and the streamtube outlet (stations r^+ and o in the same figure):

$$p_i + \frac{1}{2}\rho V_i^2 = p_{r^-} + \frac{1}{2}\rho V_{r^-}^2, \tag{12a}$$

$$p_{r^+} + \frac{1}{2}\rho V_{r^+}^2 = p_o + \frac{1}{2}\rho V_o^2, \tag{12b}$$

where p is pressure and $p_i = p_o = p_\infty$, while p_∞ is the ambient value. Additionally, $V_{r^-} = V_{r^+}$ for continuity, and furthermore $V_o^2 = u_o^2 + v_o^2$ at the outlet section, where v_o is the lateral (sidewash) speed component.

Following a customarily assumption used for helicopters rotors in forward flight (Johnson, 1995), the misaligned rotor can be seen as a lifting wing of finite span (albeit of a small aspect ratio $AR = D^2/A = 4/\pi$) operating at an angle of attack μ[1]. The chord $C(y_d)$ of the wing in the streamwise direction has an elliptic distribution: $(C(y_d)/2)^2 + y_d^2 = R^2$. According to Prandtl's lifting line theory (Tietjens and Prandtl, 1957; Katz and Plotkin, 2001), the wing has consequently an elliptic lift distribution, which induces a spanwise-constant downwash (in this case, sidewash) $v_o = \Gamma/4R$. $\Gamma = \bar{L}/\rho u_{\infty,\text{hub}}$ is the circulation at the wing mid section $y_d = 0$, and $\bar{L} = LC(0)/A$ is the lift per unit span at that same location. Since the wing lift is the rotor side force, i.e. $L = T\sin\mu$, it follows that the non-dimensional sidewash at the streamtube outlet can be expressed as

$$\frac{v_o}{u_{\infty,\text{hub}}} = \frac{1}{4}C_T\sin\mu. \tag{13}$$

Combining the previous equations, yields an expression for the 0P axial induction a_0 as a function of the misalignment μ and thrust coefficient C_T:

$$1 - a_0 = \frac{1 + \sqrt{1 - C_T - \frac{1}{16}C_T^2\sin^2\mu}}{2\left(1 + \frac{1}{16}C_T\sin^2\mu\right)}. \tag{14}$$

[1]This interpretation also reveals that the so-called curled shape of laterally deflected wakes (see e.g. Martínez-Tossas et al. (2021) and references therein) is nothing else than the effect of the horseshoe vortex structure generated behind a lifting wing, albeit with the addition of the swirl caused by the rotor rotation.

https://doi.org/10.5194/wes-2023-133
Preprint. Discussion started: 6 November 2023

eawe european academy of wind energy
Open Access WIND ENERGY SCIENCE DISCUSSIONS

2.6 Thrust force

Equation (14) furnishes an expression for the 0P axial induction as a function of the thrust coefficient. To close the problem, an expression for the thrust coefficient in terms of the operating conditions of the turbine is necessary. To this end, the thrust force T is expressed in terms of the normal sectional force F_n as

$$T = \frac{B}{2\pi}\int_0^{2\pi}\int_0^R F_n \,\mathrm{d}\psi \mathrm{d}r, \tag{15}$$

where B indicates the number of blades. Using Eq. (4b) under the assumption of a small inflow angle (i.e. $\sin\varphi \approx \varphi$ and $\cos\varphi \approx 1$), yields

$$T = \frac{B}{2\pi}\int_0^{2\pi}\int_0^R \frac{1}{2}\rho u^2 c\,(C_D\varphi + C_L)\,\mathrm{d}\psi \mathrm{d}r. \tag{16}$$

The lift coefficient can we written as $C_L = C_{L,\alpha}\alpha$, where $C_{L,\alpha}$ is the list slope, $\alpha = \varphi - \theta$ is the angle of attack, $\theta = \theta_p + \beta$ is the local pitch angle (see Fig. 3), where θ_p the blade pitch rotation at the pitch bearing and β the blade twist. Using again the small inflow angle assumption, it follows that $\varphi \approx u_p/u_t$ and $u \approx u_t$, and the thrust T becomes

$$T = \frac{B}{2\pi}\int_0^{2\pi}\int_0^R \frac{1}{2}\rho u_t^2 c\left(C_D\frac{u_n}{u_t} + C_{L,\alpha}\left(\frac{u_n}{u_t} - \theta\right)\right)\mathrm{d}\psi \mathrm{d}r. \tag{17}$$

Using Eqs. (3) and (5), solving the double integral and expressing T through the thrust coefficient $C_T = C_{T_1} + C_{T_2}$, finally gives

$$C_{T_1} = \frac{\sigma}{2}(C_D + C_{L,\alpha})\cos\mu\,(\lambda - k\cos\delta\sin\gamma)\,(1 - a_0), \tag{18a}$$

$$C_{T_2} = -\frac{\sigma}{2}C_{L,\alpha}\theta\left(\sin^2\mu + \frac{2}{3}\lambda^2 - \frac{k\cos\delta}{12}\left(8\lambda\sin\gamma - k\cos\delta(\cos^2\gamma\sin^2\delta + 3\sin^2\gamma)\right)\right), \tag{18b}$$

where $\sigma = BcR/A$ is the rotor solidity, and $\lambda = \Omega R/u_{\infty,\mathrm{hub}}$ is the tip speed ratio.

For null shear, i.e. $k = 0$, this expression simplifies to

$$C_T = \frac{\sigma}{2}\left((C_D + C_{L,\alpha})\cos\mu\left((1 - a_0)\lambda\right) - C_{L,\alpha}\theta\left(\sin^2\mu + \frac{2}{3}\lambda^2\right)\right). \tag{19}$$

Notice that the terms in Eqs. (18) depending on shear k also depend on the angles γ and δ, whereas Eq. (19) only depends on the total misalignment angle μ. This is because the wind shear is defined with respect to the ground frame, which is mapped into the nacelle frame by the γ and δ angles, whereas μ only depends on the relative orientation of the wind vector with the rotor axis, as explained in Sect.2.1.

2.7 Power

The aerodynamic power P generated by a wind turbine is $P = Q\Omega$, where the aerodynamic torque Q writes

$$Q = \frac{B}{2\pi}\int_0^{2\pi}\int_0^R F_t\, r\,\mathrm{d}\psi\,\mathrm{d}r. \tag{20}$$

https://doi.org/10.5194/wes-2023-133
Preprint. Discussion started: 6 November 2023

eawe european academy of wind energy
Open Access WIND ENERGY SCIENCE DISCUSSIONS

Considering small angles, power can be written as

$$P = \frac{B}{2\pi} \int_0^{2\pi} \int_0^R \frac{1}{2} \rho u_t^2 c \left(-C_D + C_{L,\alpha} \left(\frac{u_n}{u_t} - \theta \right) \frac{u_n}{u_t} \right) \Omega r \, \mathrm{d}\psi \mathrm{d}r. \tag{21}$$

Using Eqs. (3) and (5), expressing the angular velocity as $\Omega = \lambda u_\infty / R$, and solving the double integral yields the power coefficient C_P:

$$\begin{aligned} C_P = \frac{\sigma}{2} \lambda \Bigg(& C_{L,\alpha}(1-a_0)\cos\mu \left((1-a_0)\cos\mu - \frac{2}{3}\lambda\theta \right) - \frac{1}{2} C_D (\lambda^2 + \sin^2\mu) \\ & + k\cos\delta\sin\gamma \left(\frac{2}{3}\cos\mu C_{L,\alpha}\theta(1-a_0) - \frac{1}{2}\lambda C_D \right) \\ & + \frac{1}{4}k^2\cos^2\delta \left(\cos^2\mu C_{L,\alpha}(1-a_0)^2 - \frac{1}{4} C_D (\sin^2\mu + 2\sin^2\gamma) \right) \Bigg). \end{aligned} \tag{22}$$

For null shear, i.e. $k = 0$, the power coefficient simplifies to

$$C_P = \frac{\sigma}{2} \lambda \left(C_{L,\alpha}(1-a_0)\cos\mu \left((1-a_0)\cos\mu - \frac{2}{3}\lambda\theta \right) - \frac{1}{2} C_D (\lambda^2 + \sin^2\mu) \right). \tag{23}$$

Due to the explicit dependency of C_P on $\cos\mu$ and of $1 - a_0$ on $\sin^2\mu$ (see Eq. 14), it follows that – in an unsheared inflow – the aerodynamic power does not depend on the misalignment direction.

2.8 Dependency on misalignment direction

The power model reveals that vertical shear is the culprit for the observed lack of symmetry with respect to yaw misalignment. In fact, because of the second term in Eq. (22) (which is proportional to $k\sin\gamma$), yawing a rotor out of the wind in a sheared inflow will produce a non-symmetric behavior with respect to positive and negative yaw angles γ, i.e. $P(-\gamma) \neq P(+\gamma)$. The yaw angle sign associated with the larger power capture depends on the balance of multiple terms, which in turn depend on some rotor design parameters but also on the pitch setting θ and tip speed ratio λ. For negative or low θ, negative yaw angles can lead to slightly higher power, whereas for increasing pitch – and hence a reduced thrust coefficient –, positive yaw angles produce more. This complex balance of effects is probably the cause for the lack of agreement in the literature on which misalignment direction yields more. As shown by the model, there is no simple answer, and the behavior depends on the rotor design and on how it is operated.

Very similar conclusions apply also to the thrust coefficient. According to Eqs. (18), $C_{T_1}(-\gamma) > C_{T_1}(+\gamma)$, because C_{T_1} depends on $-k\sin\gamma$; whereas $C_{T_2}(-\gamma) < C_{T_2}(+\gamma)$ (when $\theta > 0$), because C_{T_2} depends on $+\theta k\sin\gamma$. Therefore one can expect a slightly higher thrust for negative yaw angles at low pitch settings, and viceversa at the higher pitch values (the effect being more pronounced at larger tip speed ratios).

To illustrate these findings in an exemplary case, Fig. 5 shows the thrust and power coefficients as functions of the misalignment angle γ, for different shear coefficients k and blade pitch angles θ. All coefficients have been normalized by their respective value in aligned conditions.

https://doi.org/10.5194/wes-2023-133
Preprint. Discussion started: 6 November 2023

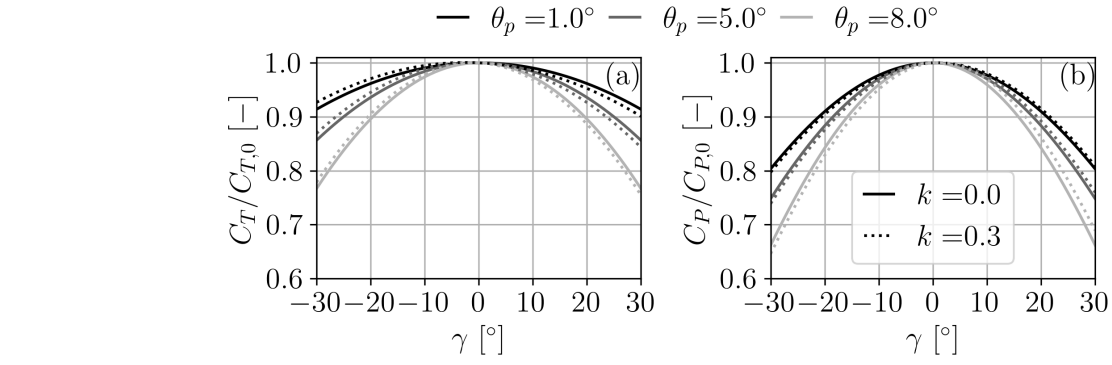

Figure 5. Normalized thrust C_T/C_{T_0} **(a)** and power C_P/C_{P_0} **(b)** coefficients, plotted as functions of the misalignment angle γ, for different shear coefficients k and pitch angles θ. $C_{T,0}$ and $C_{P,0}$ respectively indicate the thrust and power coefficients in aligned conditions, i.e. for $\gamma = 0$. The plots were generated considering the following values: $\lambda = 8.5$, $C_D = 4.4 \times 10^{-3}$, $C_{L,\alpha} = 4.82$, $\beta = -3.16°$, $\sigma = 4.16\%$, $\delta = -5°$, $R = 65$ m. An interactive version of the figure that allows to plot the thrust and power coefficients for user-defined values of the model parameters is available as a Jupyter notebook at the link https://tinyurl.com/btcl-fig5.

The lack of symmetry of the rotor with respect to misalignment direction is in general rather small. In a typical field implementation of wake steering, various uncertainties – e.g., due to limits in the knowledge of the ambient conditions, actual yaw orientation of the rotor, asymmetric behavior of the onboard anemometry, etc. – and other model errors probably dominate the problem, making the asymmetric behavior of misalignment a negligible effect, especially for small pitch values and moderate tip speed ratios.

The analysis can be conducted also for a horizontal shear, for example as produced by a wake impingement, leading to similar conclusions.

2.9 Implementation

The analytical model derived in the previous pages can be readily implemented in engineering flow models (NREL, 2023b; Pedersen et al., 2019). An open-source implementation in FLORIS (NREL, 2023b) is available on Github (Tamaro et al., 2023). As a summary, we report here for convenience the governing Eqs. (14) and (18), which write

$$1 - a_0 = \frac{1 + \sqrt{1 - C_T - \frac{1}{16} C_T^2 \sin^2 \mu}}{2\left(1 + \frac{1}{16} C_T \sin^2 \mu\right)}, \tag{24a}$$

$$C_T = \frac{\sigma}{2}\Bigg((C_D + C_{L,\alpha}) \cos\mu \left(\lambda - \cos\delta \sin\gamma k\right) (1 - a) -$$

https://doi.org/10.5194/wes-2023-133
Preprint. Discussion started: 6 November 2023

eawe european academy of wind energy
Open Access WIND ENERGY SCIENCE DISCUSSIONS

$$C_{L,\alpha}\,\theta\left(\sin^2\mu+\frac{2}{3}\lambda^2-\frac{k\cos\delta}{12}\left(8\lambda\sin\gamma-k\cos\delta(\cos^2\gamma\sin^2\delta+3\sin^2\gamma)\right)\right)\Bigg). \tag{24b}$$

This represents a closed system of equations that can be solved for the axial induction a_0 and thrust coefficient C_T, given the yaw misalignment γ, pitch setting θ, and tip speed ratio λ. The solving system depends also on the parameters σ, C_D, $C_{L,\alpha}$, β. Having obtained a_0 and C_T, the rotor power is finally obtained as

$$P(\gamma,\theta,\lambda)=\frac{1}{2}\rho A u^3_{\infty,\text{hub}}C_P(\gamma,\delta,\theta,\lambda), \tag{25}$$

where C_P is given by Eq. (22).

It should be noted that, through Eq. (24b) and (25), the analytical model depends on C_D, $C_{L,\alpha}$ and β. These are average parameters, which represent in the model the "equivalent" effect caused by corresponding quantities that in reality vary spanwise (but possibly also azimuthally) over the rotor disk. Furthermore, the analytical derivation of the equations implies that the model lacks many of the features that are present in more sophisticated BEM implementations, such as radially and azimuthally non-uniform induction, swirl induction, tip and root losses, radial flow, spanwise varying geometric characteristics, prebend, etc. Clearly, this lack of accuracy could be resolved by numerically implementing the same model in a BEM code (Hansen, 2015). However, this way the use of the misaligned rotor model in combination with an engineering wake model would become much more complex and numerically expensive.

To address this problem, the following implementation is recommended, which was used in the validation and the examples reported in the following section.

First, the power loss function η_P is computed by using Eqs. (24) and (25) to yield

$$\eta_P(\gamma,\delta,\theta,\lambda)=\frac{P(\gamma,\delta,\theta,\lambda)}{P(0,\delta,\theta,\lambda)}. \tag{26}$$

Next, a refined power estimate P' is obtained as

$$P'(\gamma,\delta,\theta,\lambda)=\eta_P(\gamma,\delta,\theta,\lambda)P^*(0,\delta,\theta,\lambda), \tag{27}$$

where P^* is the power computed in aligned conditions through a higher-fidelity model, for example based on a sophisticated BEM implementation or even on experimental measurements, when available. In other words, the analytical model is used not to predict the actual power output, but only the fraction of power that is lost by misalignment. The actual total capture is obtained by applying the loss model to a more accurate power model in aligned conditions. The same approach is adopted for thrust: a thrust change factor is computed through the model as $\eta_T(\gamma,\theta,\lambda)=T(\gamma,\theta,\lambda)/T(0,\theta,\lambda)$, and a refined thrust estimate in misaligned conditions is obtained as $T'(\gamma,\theta,\lambda)=\eta_T(\gamma,\theta,\lambda)T^*(0,\theta,\lambda)$ from a higher-fidelity aligned thrust model T^*.

The parameters C_D, $C_{L,\alpha}$, and β are calibrated to minimize the error produced by the model in the prediction of the power loss factor η_P and of the thrust coefficient C_T. Notice that C_T is preferred to η_T for this scope, because it was found that the informational content of η_T is very similar to the one of η_P, reducing the quality of the tuning.

Tuning is performed by numerically solving the following minimization problem

$$\min_{C_D,C_{L,\alpha},\beta}\quad\sqrt{\frac{1}{N}\sum_{i=1}^{N}\left(\eta^{\text{obs}}_{P,i}-\eta^{\text{mod}}_{P,i}\right)^2}+\sqrt{\frac{1}{N}\sum_{i=1}^{N}\left(C^{\text{obs}}_{T,i}-C^{\text{mod}}_{T,i}\right)^2}, \tag{28}$$

https://doi.org/10.5194/wes-2023-133
Preprint. Discussion started: 6 November 2023

eawe european academy of wind energy
Open Access WIND ENERGY SCIENCE DISCUSSIONS

where $(\cdot)_i^{\text{obs}}$ are N numerical or experimental observations, and $(\cdot)_i^{\text{mod}}$ the corresponding model predictions. For each data set, tuning was performed solving $N/2$ times problem (28) using a gradient based optimization, each time with a different random 50% subset of the available data, and finally averaging the resulting parameters.

3 Model validation

3.1 LES-ALM numerical model

LES-ALM simulations are used for testing the accuracy of the model in representing misaligned conditions, similarly to what done by other authors (Gebraad et al., 2016; Liew et al., 2020; Nanos et al., 2022). The effects of the rotor on the flow are modelled with the filtered ALM of Troldborg et al. (2007) and Martínez-Tossas and Meneveau (2019), by projecting forces computed along the lifting lines onto the LES grid. The Cartesian mesh consists of approximately 3.5 million cells, and uses four refinement levels. The smallest cells measure 1 m, and are located in correspondence of the rotor.

Table 1. Operational scenarios for the LES-ALM simulations.

Scenario #	1	2	3	4
λ [-]	8	9.5	8.38	8.38
k [-]	0	0	0.06	0.19
θ_p [deg]	Varied to modify C_T			

Simulations were conducted for the IEA 3.4 MW reference wind turbine, a typical onshore machine with contemporary design characteristics. The technical specifications of the machine are reported in Bortolotti et al. (2019). Here we only note that the turbine has a 5° uptilt angle, i.e. $\delta = -5°$. The four operational scenarios of Table 1 were considered, each corresponding to a different tip speed ratio λ and shear coefficient k. The flow is steady in all scenarios, but only cases 3 and 4 represent a sheared inflow, as shown in Fig. 6. In each scenario, the thrust coefficient was changed by varying the pitch angle according to the values $\theta_p = \{1.4, 4.9, 6.7, 8.1\}°$, using the derating controller of Campagnolo et al. (2023).

The model parameters were calibrated as explained in Sect. 2.9, obtaining the values $C_D = 0.0040 \pm 0.0001$, $C_{L,\alpha} = 4.796 \pm 0.038$ rad^{-1}, $\beta = -3.177 \pm 0.005°$, with a 95% confidence level.

Figure 7 reports the power loss factor η_P in the range of yaw misalignment $-30° < \gamma < 30°$, for the four scenarios of Table 1 and different pitch settings. Model predictions are indicated with lines, and LES-ALM results with markers.

Overall, there is a very good match between model predictions and numerical simulations. Results for inflow scenarios 1 and 2, which are characterized by a null vertical shear (see Fig. 6), are reported in Figs. 7a and 7b. As predicted by the model, in these cases power is symmetric with respect to positive and negative yaw angles. On the other hand, power is not symmetric in Figs. 7c and 7d, which correspond to the sheared inflow cases of scenarios 3 and 4. In particular, Fig. 7c shows clear evidence of the complex behavior described in Sect. 2.8. At high C_T (low pitch), the curve is very nearly symmetric with respect to γ. However, as thrust is decreased (and pitch increased), power capture at positive γ values is larger than for negative

https://doi.org/10.5194/wes-2023-133
Preprint. Discussion started: 6 November 2023

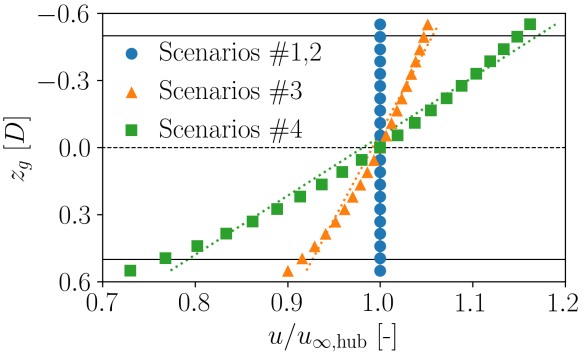

Figure 6. Vertical inflow wind speed profiles used in the LES-ALM simulations, with corresponding best-fitted linear shears (dotted lines).

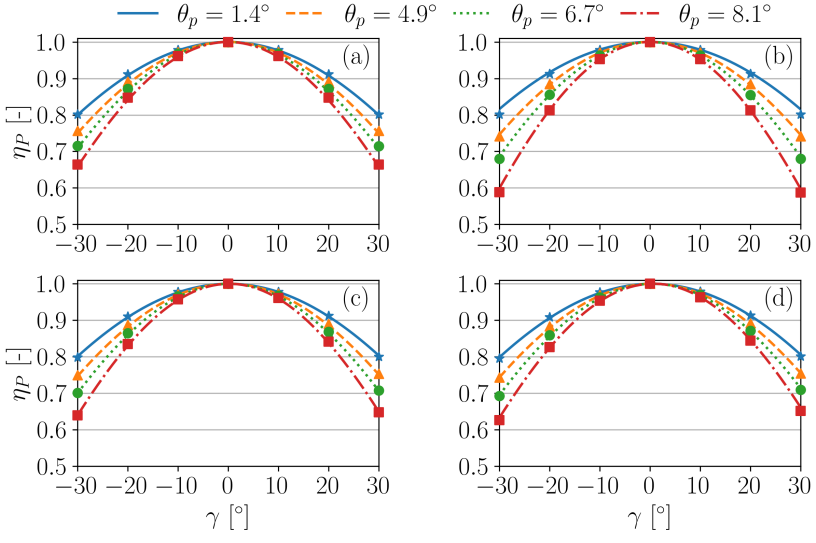

Figure 7. Power loss factor η_P vs. misalignment angle γ. Model predictions: lines; LES-ALM simulations: markers. The different line and marker styles correspond to the different thrust coefficients C_T. Scenario 1 **(a)**; scenario 2 **(b)**; scenario 3 **(c)**; scenario 4 **(d)**.

https://doi.org/10.5194/wes-2023-133
Preprint. Discussion started: 6 November 2023

eawe european academy of wind energy
Open Access WIND ENERGY SCIENCE DISCUSSIONS

misalignments. As predicted by the model, this effect is more visible in Fig. 7c than in Fig. 7d, because the former has a higher tip speed ratio than the latter (see Table 1 and the explanation given in Sect. 2.8).

The results of Fig. 7 clearly indicate a strong dependency of the power loss factor on the trust coefficient. This can be appreciated even more clearly in Fig. 8, where the results for all scenarios at $\gamma = \pm 30°$ were interpolated to plot the average $\bar{\eta}_P$ as a function of λ for four different values of the thrust coefficient. The plot clearly shows that low C_T values increase power losses in misaligned conditions, in agreement with Heck et al. (2022) and Campagnolo et al. (2023). Similarly, the tip speed ratio has also a strong influence on power losses, which decrease when λ is reduced.

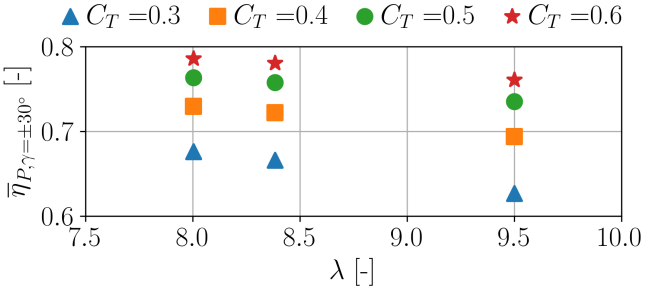

Figure 8. Power loss factor $\bar{\eta}_P$ (averaged among all scenarios) at misalignments $\gamma = \pm 30°$ vs. tip speed ratio λ, for varying thrust coefficient C_T.

Figure 9 reports the thrust change factor η_T as a function of yaw misalignment, for the same four scenarios and different thrust settings. Here again, model predictions are indicated with lines, and LES-ALM results with markers. There is a consistently good match, for all scenarios, and for all yaw and pitch values. The lack of symmetry is again consistent with the model, similarly to the case of power discussed above. Figure 9c shows a higher thrust for positive yaw angles at low thrust coefficients (high pitch values), because of the high tip speed ratio of scenario 3, indicating that term C_{T_2} prevails over C_{T_1}. The opposite happens in Fig. 9d, due to the lower λ of scenario 4.

Overall, it appears that the performance of the rotor is strongly dependent on the way it is controlled when it yaws out of the wind. Hence, the standard power law $\cos^{p_p}$ may oversimplify the complex aerodynamics that are typical of this problem. On the other hand, notwithstanding its simplicity, the proposed model is in very good agreement with sophisticated CFD simulations, and is capable of describing even relatively minor effects of the complex behavior of a misaligned wind turbine rotor in a sheared inflow.

3.2 Wind tunnel measurements

Next, the model is compared to data recorded during wind tunnel experimental campaigns performed with a G1 wind turbine (Campagnolo et al., 2016). This scaled machine has a diameter of 1.1 m, a rated rotor speed of 850 RPM, and null tilt. The

https://doi.org/10.5194/wes-2023-133
Preprint. Discussion started: 6 November 2023

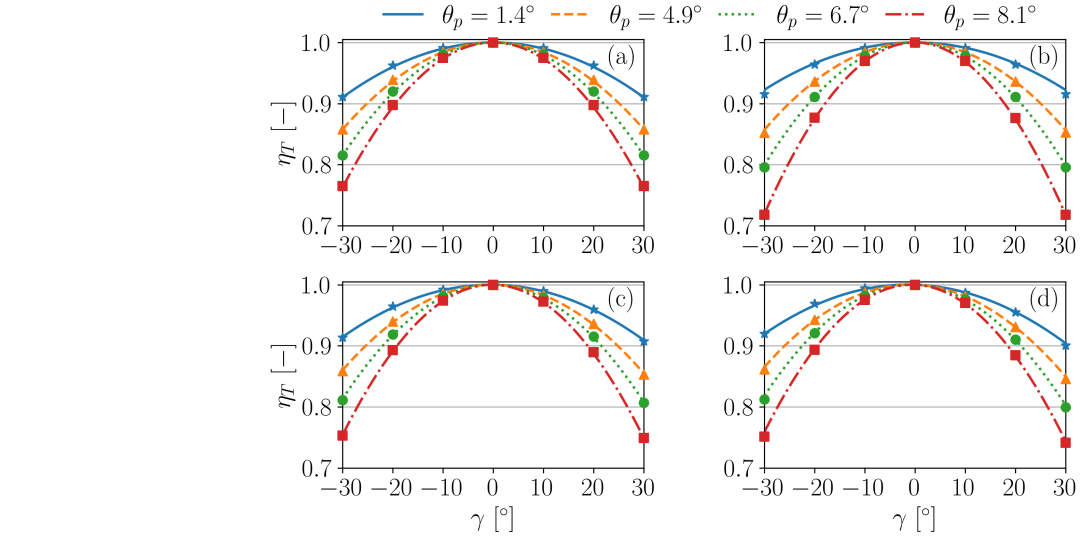

Figure 9. Thrust change factor η_T vs. misalignment angle γ. Model predictions: lines; LES-ALM simulations: markers. The different line and marker styles correspond to the different pitch settings. Scenario 1 **(a)**; scenario 2 **(b)**; scenario 3 **(c)**; scenario 4 **(d)**.

design of the G1 is described in Bottasso and Campagnolo (2022b), and its rotor aerodynamic and wake characteristics have been reported in Wang et al. (2021) and references therein.

Tests were performed in a boundary layer wind tunnel (Bottasso et al., 2014) with three different inflows: the first one, termed Low-TI, has no shear and a very low turbulence intensity (approx. 1%); the other two, termed Mod-TI and High-TI, have respectively TIs of approx. 6% and 13% at hub height, and vertical linear shears in the rotor region equal to $k = 0.11$ and $k = 0.15$, respectively. Figure 10a reports the vertical profiles of the longitudinal wind speed component u measured by means of CTA probes (Bottasso et al., 2014), normalized by the wind speed u_{pitot} measured by a Pitot tube placed at hub height. Figure 10b shows the vertical profiles of the turbulence intensity, as measured with the same instrumentation.

Two different campaigns were conducted for characterizing power losses in misaligned conditions: in the first one the turbine was set at full power, whereas in the second at different levels of derating. For the second campaign the turbine was derated in the range $P_d \in [50, 100]\%$ while adopting two different strategies: iso-λ, where the tip speed ratio is held constant (Campagnolo et al., 2023), and min-C_T, where the thrust coefficient is minimized (Juangarcia et al., 2018). The first campaign was conducted in all three Low-TI, Mod-TI, and High-TI inflow conditions, with hub-height wind speeds of 5.86, 5.69, and 5.40 ms^{-1}, respectively. The second campaign was conducted only in the Mod-TI inflow, with a hub-height wind speed of 5.62 ms^{-1}. All test conditions correspond to region II operation, i.e. the below-rated partial-load regime of the turbine.

Various sources of error affect the experimental observations. These include measurements of the wind speed u_{pitot} upstream of the model (obtained by a Pitot tube placed at hub height 3D in front of the turbine), of the air density ρ, of the rotor speed Ω, of the shaft torque Q, of the bending moment at tower base (which is used to estimate thrust), and of the nacelle orientation with

https://doi.org/10.5194/wes-2023-133
Preprint. Discussion started: 6 November 2023

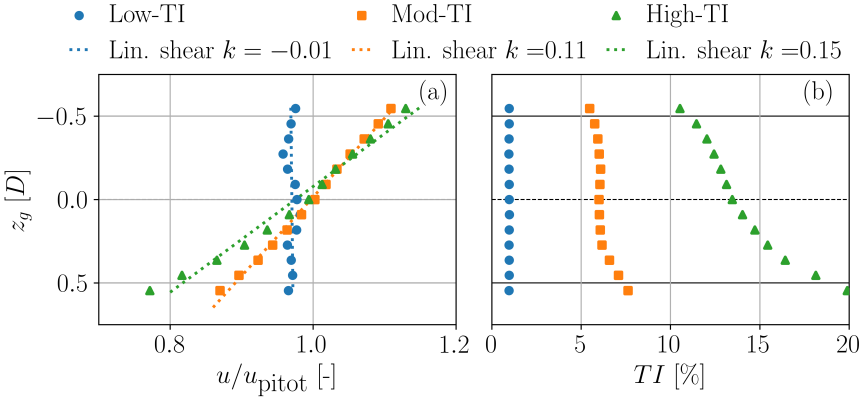

Figure 10. Wind tunnel inflows. Vertical wind speed profiles, with corresponding best-fitted linear shears (dotted lines) **(a)**; vertical profiles of turbulence intensity **(b)**.

respect to the wind tunnel. The error in u_{pitot} is related to the uncertainty associated with the measurements of flow density and dynamic pressure. This latter is measured with a MKS Baratron-Type 226A transducer (Baratron, 2022) with full span equal to 1 Torr, characterized by an accuracy of ± 0.4 Pa. Density is instead derived from measurements of air pressure, temperature and humidity, and it is affected by an error equal to ± 0.01 kgm^3 (Wang et al., 2020). Torque is measured with a load cell installed on the rotor shaft, and it is affected by an uncertainty of ± 0.005 Nm. The rotor speed measurement, provided by an optical incremental encoder, is instead affected by an error equal to ± 1.5 RPM. The measurement uncertainty on power $P = Q\Omega$ is derived by adding in quadrature the uncertainties on Q and Ω. Finally, thrust T is obtained by correcting the measurements of the bending moments at tower base by the effects induced by the drag of the tower, nacelle and hub spinner (Wang et al., 2020). The calibration of the load cell at tower base reveled an uncertainty on the thrust of ± 0.14 N. In turn, all these effects are used to quantify uncertainties in the tip speed ratio λ, thrust coefficient C_T, and yaw-induced power losses η_P, again by adding errors in quadrature.

In the two test campaigns, 94 observations were conducted, each one for a duration of 2 minutes. The measured average θ_p and λ are reported in Appendix B, and were used as inputs to the model equations.

Given the small size of the G1 wind turbine, the Reynolds number at its blade sections is particularly low. Although special low-Reynolds airfoils are used in the design of the G1 blades (Bottasso and Campagnolo, 2022b), their lift and drag coefficients are particularly sensitive to the operating conditions of the turbine (Wang et al., 2020). In order to account for this effect, the model parameters C_D and $C_{L,\alpha}$ are assumed to depend on the rotational speed Ω, since the relative speed at the airfoils is close to the tangential speed ($u \approx u_t$, see Fig. 3). Tuning was performed with Eq. (28), using as unknown parameters the values of C_D and $C_{L,\alpha}$ at $\Omega = [850, 625, 400]$ RPM; a piecewise linear interpolation was used at other intermediate values of the rotor speed. Clearly, it is not necessary to consider a Reynolds-dependency for β, and therefore a single value for this parameter was considered. Figure 11 reports the tuned C_D and $C_{L,\alpha}$ parameters, the shaded areas representing the corresponding 95%

https://doi.org/10.5194/wes-2023-133
Preprint. Discussion started: 6 November 2023

eawe european academy of wind energy
Open Access WIND ENERGY SCIENCE DISCUSSIONS

385 confidence intervals. As expected, drag decreases whereas lift slope increases for increasing rotor speed, i.e. for increasing sectional Reynolds number. The tuned twist β is equal to $1.4472 \pm 0.1408°$.

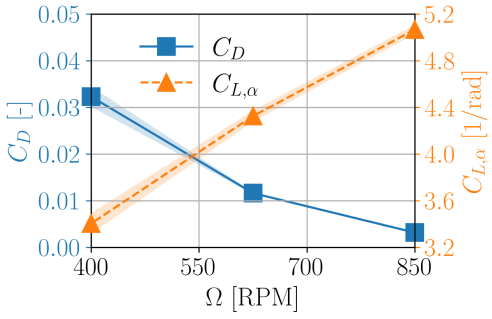

Figure 11. Tuned model parameters C_D and $C_{L,\alpha}$ as functions of rotational speed Ω.

For full-power operation (first test campaign), Fig. 12 reports a comparison between model-predicted (lines) and measured (markers) power losses and thrust coefficients. There is a good match between experiment and model, the latter falling within the uncertainty range of the measurements in most cases. As predicted by the model, the sheared inflow conditions Mod-TI 390 and High-TI exhibit the expected non-symmetric behavior with respect to positive and negative yaw angles.

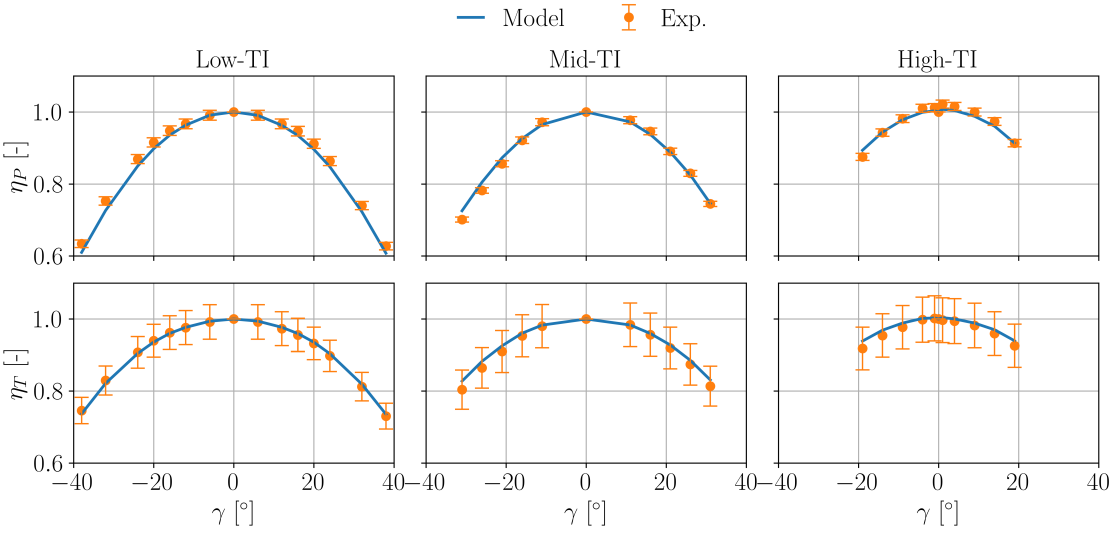

Figure 12. Power loss factor η_P (top row) and thrust change factor η_T (bottom row) vs. yaw misalignment γ, in full-power operation for the three different inflows. Model predictions: solid lines; experiments: markers. The bars indicate measurement uncertainties.

https://doi.org/10.5194/wes-2023-133
Preprint. Discussion started: 6 November 2023

eawe european academy of wind energy
Open Access WIND ENERGY SCIENCE DISCUSSIONS

The same quantities are reported for derated operation (second test campaign) in Fig. 13. Here again the match between experimental data and model predictions is very good, the latter being mostly within the uncertainty band of the measurements. Slightly larger deviations are observed for the min-C_T case at P_d=50%. This can be explained by the fact that the machine operates at significantly low λ values, with consequent low rotational speeds. This results in particularly high angles of attack (Juangarcia et al., 2018) and very low chord-based Reynolds. Both have significant impacts on the airfoil performance, which are likely not properly captured by the analytical model. Overall, it appears that the model is capable of capturing the reduction in the thrust coefficient as derating P_d increases, as well as the lack of symmetry with respect to the misalignment angle.

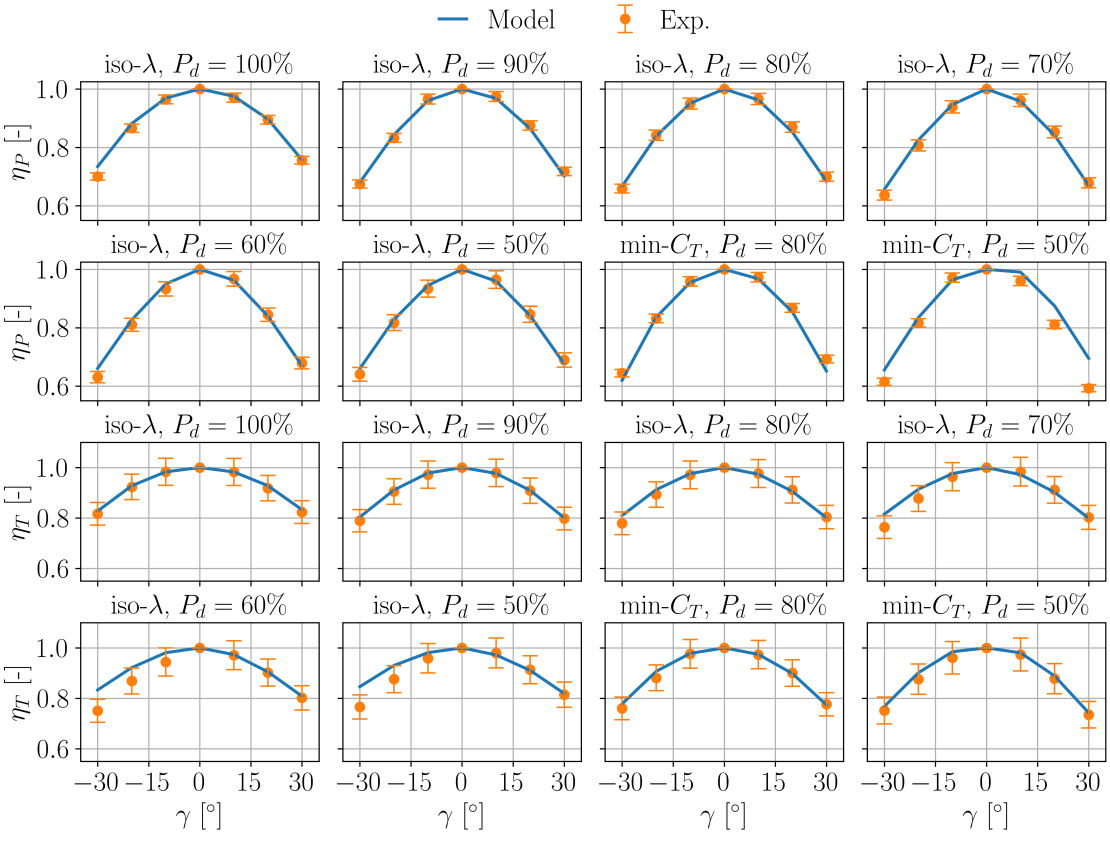

Figure 13. Power loss factor η_P (two top rows) and thrust change factor η_T (two bottom rows) vs. yaw misalignment γ, in derated operation for the Mid-TI inflow case. Model predictions: solid lines; experiments: markers. The bars indicate measurement uncertainties.

4 Optimal wake steering

The insight provided by the new model suggests two questions:

https://doi.org/10.5194/wes-2023-133
Preprint. Discussion started: 6 November 2023

eawe european academy of wind energy
Open Access WIND ENERGY SCIENCE DISCUSSIONS

- What is the power-optimal way to yaw a single turbine out of the wind?
- And does the new model affect the way wake steering should be conducted?

We try to give some initial answers to these questions in the following two sections.

4.1 Optimal power capture of a single misaligned turbine

The new model was used to compute the optimal power of a wind turbine when it is misaligned with respect to the wind. The analysis was conducted for the same IEA 3.4 MW wind turbine used for the previous numerical validation of the model.

The optimal control strategy was computed by numerical optimization using an adaptive Nelder-Mead algorithm (Gao and Han, 2012), and results are shown in Fig. 14. The figure reports also the standard region II control approach, which consists in holding the pitch angle fixed while the generator torque is varied proportionally to the square of the rotor speed, i.e. $Q \sim \Omega^2$. Assuming as a first approximation that $P = \cos\gamma^{p_p}$, and considering that $Q = P/\Omega$, it follows that $\Omega \sim \cos\gamma^{p_p/3}$. The figure reports the solution computed for a coefficient $p_p = 1.88$, following Fleming et al. (2015).

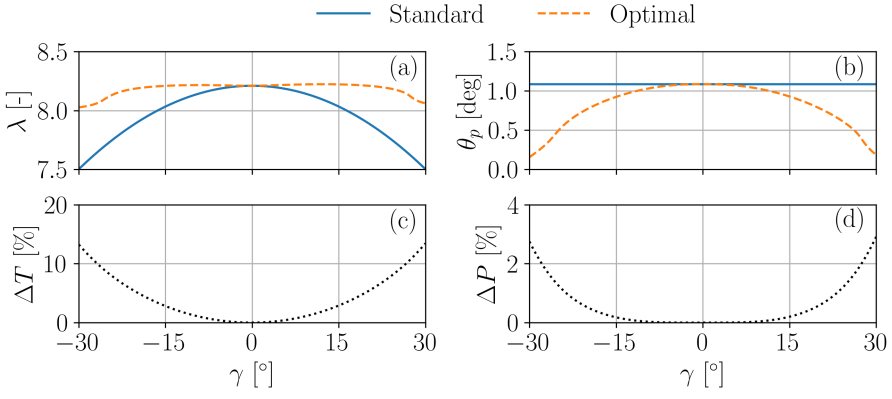

Figure 14. Comparison between standard and optimal control strategies for different yaw angles γ. Tip speed ratio λ **(a)**; pitch angle θ_p **(b)**; thrust difference between the optimal and standard strategies **(c)**; power difference between the optimal and standard strategies **(d)**.

As the yaw misalignment increases, the tip speed ratio drops for the standard control strategy, driven by the reduced rotor-orthogonal component of the wind. Since the pitch angle remains fixed, the reduced λ leads also to a decreased thrust coefficient. Although this might be beneficial for reducing loading on the yawed turbine, the resulting drop in power is significant. On the other hand, the optimal strategy governs the turbine to keep a much more constant tip speed ratio and thrust coefficient, while the blade pitches back a little. This results into some power boost, which is small for moderate angles but reaches above 3% around $\pm 30°$. While the higher C_T implies that the turbine is loaded more than in the standard case, it has also an effect on the wake that will be felt downstream, as explored in the next section.

https://doi.org/10.5194/wes-2023-133
Preprint. Discussion started: 6 November 2023

eawe european academy of wind energy
Open Access WIND ENERGY SCIENCE DISCUSSIONS

4.2 Optimal power capture of two turbines

FLORIS v3 (NREL, 2023b), modified with the present model, was used to optimize the power capture of a cluster of two IEA 3.4 MW wind turbines placed at a distance of 5 diameters. The wake was modelled with the Gauss-Curl-Hybrid model (King et al., 2021). The inflow is characterized by an ambient wind speed $u_{\infty,\mathrm{hub}} = 9.7$ ms^{-1}, a shear of 0.12, a turbulence intensity of 6%, and a 60° range of wind directions Φ to realize different degrees of overlap between the wake and the downstream rotor. The optimal wind farm control strategy was computed by numerically maximizing the cluster power with the same adaptive Nelder-Mead algorithm used for the single-turbine case of the previous section.

Results are shown in Fig. 15. The plots report in green the results obtained with greedy control (i.e., each turbine maximizes its own power capture), in blue the solution obtained with wake steering control based on the $\cos^{p_p}$ law using $p_p = 1.88$, and in orange with wake steering control based on the present model. For the three control strategies, results were validated with LES-ALM simulations run for five different wind directions, namely $\Phi = \{270 \pm 5.74, 270 \pm 2.5, 270\}°$, corresponding to rotor overlaps of 50%, 78.2%, and 100%, respectively. The LES-ALM results are indicated in the figure with markers, where the colors correspond to the control strategy.

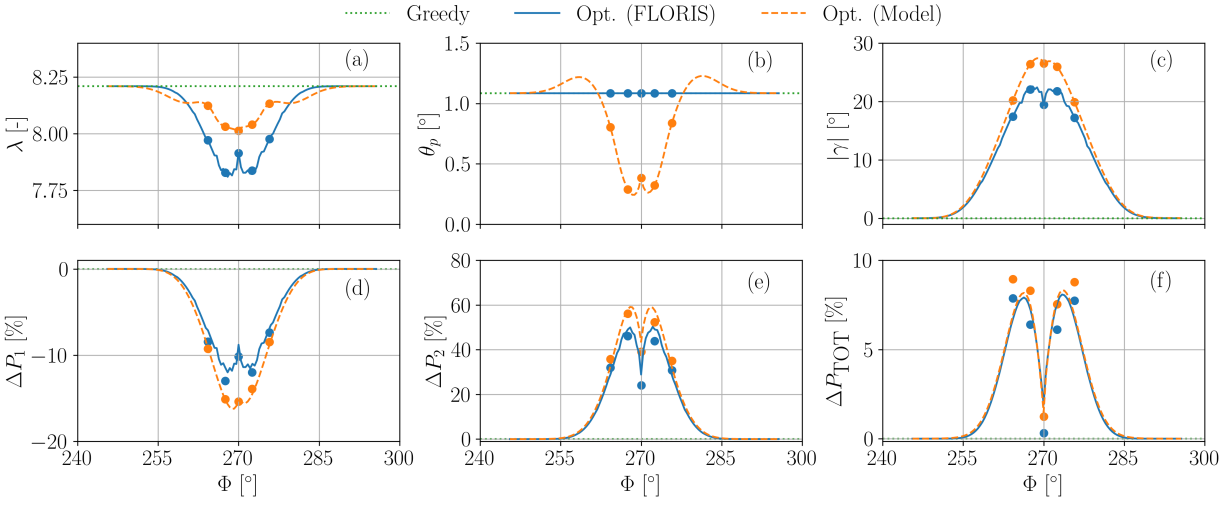

Figure 15. Control of a cluster of two turbines in wake interference conditions. Green: greedy policy; blue: optimal wake steering solution based on $\cos^{p_p}$; orange: optimal wake steering solution based on new model. Lines: FLORIS engineering wake model; markers: LES-ALM CFD. Tip speed ratio λ **(a)**; thrust coefficient C_T **(b)**; absolute yaw misalignment $|\gamma|$ **(c)**; power changes with respect to the greedy policy for the upstream wake-steering turbine **(d)**; power changes with respect to the greedy policy for the downstream turbine **(e)**; overall power changes for the cluster of two turbines **(f)**.

Figures 15a, 15b, and 15c respectively show the front turbine tip speed ratio λ, pitch angle θ_p, and absolute misalignment angle $|\gamma|$, all plotted as functions of wind direction Φ. The solution for the present model is characterized by a fairly constant

https://doi.org/10.5194/wes-2023-133
Preprint. Discussion started: 6 November 2023

eawe european academy of wind energy
Open Access WIND ENERGY SCIENCE DISCUSSIONS

tip speed ratio that, in conjunction with some pitch back of the blades at the highest misalignments, results also in a roughly constant thrust coefficient (not shown for brevity). This is in contrast with the solution based on the $\cos^{p_p}$ law, where both tip speed ratio and thrust coefficient drop at the higher misalignments that correspond to the strongest wake overlap conditions. In addition, the present model also results into slightly larger misalignment angles, as shown by Fig. 15c.

The bottom three plots show the effects of the various control strategies on power as function of wind direction Φ. Figures 15d and 15e report the power changes with respect to the greedy strategy for the front and back turbines, respectively. It appears that the upstream machine, thanks to a higher tip speed ratio and different pitch control, looses less power than in the $\cos^{p_p}$ case. Additionally, it also appears that the second machine gains more power with the strategy based on the new model, thanks to a higher misalignment of the upstream turbine but also due to its larger thrust coefficient. Finally, Fig. 15f shows the overall gain at the cluster level. Results indicate a fairly consistent improvement, in excess of roughly 1%, for almost the entire wake-overlap range.

The LES-ALM results confirm the findings based on the FLORIS engineering wake model: less power losses for the front turbine, and more gains for the downstream one.

5 Conclusions

We have presented a new model to estimate the power performance of a misaligned wind turbine rotor. The model is a modified version of the classical blade element momentum theory, where the rotor is considered as a lifting wing of finite span operating at an angle of attack.

The new model reveals the following characteristics of the behavior of a misaligned rotor:

- Power does not depend on the misalignment angle according to the $\cos^{p_p}$ law, a formula in widespread use in the literature.
- The true effective misalignment angle that drives wake behavior is a combination of both yaw and tilt. Therefore, a two-dimensional wake model should be described in the plane formed by the rotor axis and wind vectors, not on the horizontal plane as commonly assumed.
- Power depends on the true misalignment angle, but – crucially – also on the way the rotor is governed as it is pointed out of the wind, a fact that probably explains the widely different performance observed by various authors. This fact also means that power losses due to misalignment can be mitigated by using a suitable control strategy.
- According to the model, the observed lack of symmetry between positive and negative misalignment angles is caused by the interaction with a sheared inflow. In these conditions, there is a complex interplay of various effects that may lead to various outcomes in terms of which yaw sign yields more or less power. In general, one can expect a small asymmetry at high thrust coefficients, while a more pronounced asymmetry emerges for low thrust and high tip speed ratios, where a higher power is generated for positive yaw angles. However, in general the behavior of power (but of thrust too, which also exhibits an asymmetric behavior) depends not only on the rotor design characteristics but also on the way it is

https://doi.org/10.5194/wes-2023-133
Preprint. Discussion started: 6 November 2023

governed, through the values of the pitch setting and of the tip speed ratio. Additionally, in the field other effects may be present (e.g., due to an asymmetric behavior of the onboard wind vane), which may add to the phenomena described by the model.

– A constant-over-the-rotor induction is sufficient to accurately describe the power and thrust behavior of a misaligned rotor in a sheared inflow. In fact, under classical small angle assumptions, the tilting of the inflow due to misalignment and shear has only a negligible effect on the quality of the results.

The model was derived in a semi-analytical form, leading to a closed system of equations that can be directly integrated with engineering wake models, at an irrelevant computational cost. To improve its accuracy, we proposed a specific implementation that overcomes the intrinsic limits brought by the analytical solution of some model integrals. The proposed implementation corrects for the effects of misalignment a higher-fidelity power model obtained in aligned conditions, and calibrates the model parameters based on measurements.

The model was validated in a broad range of cases, considering LES-ALM numerical simulations of a multi-MW machine as well as experimental observations on a scaled wind tunnel model, in different inflows (from unsheared laminar to sheared highly turbulent conditions), in full-power and derated conditions. In all cases, the model achieved a very satisfactory agreement with the numerical and experimental reference values.

Using the proposed model, we maximized the power capture of a wind turbine for a range of misalignment angles, obtaining the optimal power strategy in terms of pitch setting and tip speed ratio. Results indicate that the maximum power extraction is obtained by keeping an almost constant tip speed ratio and by slightly reducing the blade pitch as the turbine yaws out of the wind. This also implies a roughly constant thrust coefficient, which will increase the loading on the yawed turbine, but will also have an effect on its wake.

Next, we applied the new model to the maximization of the power by wake steering for a cluster of two turbines. The resulting control strategy was compared to the one obtained by the classical $\cos^{p_p}$ power loss model, and validated by means of LES-ALM simulations for a few selected cases. Results indicate that the proposed model results in smaller power losses for the wake-steering turbine, and greater power gains for the wake-affected one, achieving a small but consistent gain in power at the cluster level for the full range of possible wake overlaps.

Future work should investigate the effects of the new model and its resulting control strategy in more complex conditions. Of particular interest is the analysis of the effects on loads, which might increase because of the eliminated drop in thrust coefficient as the turbine is yawed out of the wind.

Appendix A: Transformation matrices

A1 Transformation from ground to nacelle frame of reference

The nacelle-fixed frame of reference is obtained from the ground-fixed frame by a first rotation δ about the horizontal axis $\boldsymbol{y}_g$, followed by a rotation γ about the vertical axis $\boldsymbol{z}_g$. The components of a generic vector $\boldsymbol{v}$ are noted $\underline{v}_g$ when measured in the

https://doi.org/10.5194/wes-2023-133
Preprint. Discussion started: 6 November 2023

eawe european academy of wind energy
Open Access WIND ENERGY SCIENCE DISCUSSIONS

ground frame $\mathcal{F}_g$, and $\underline{v}_n$ when measured in the nacelle frame $\mathcal{F}_n$. Combining the two successive rotations, one obtains the transformation of components from one frame to the other as

$$\underline{v}_n = \begin{bmatrix} \cos\delta & 0 & -\sin\delta \\ 0 & 1 & 0 \\ \sin\delta & 0 & \cos\delta \end{bmatrix} \begin{bmatrix} \cos\gamma & -\sin\gamma & 0 \\ \sin\gamma & \cos\gamma & 0 \\ 0 & 0 & 1 \end{bmatrix} \underline{v}_g = \begin{bmatrix} \cos\delta\cos\gamma & -\cos\delta\sin\gamma & -\sin\delta \\ \sin\gamma & \cos\gamma & 0 \\ \sin\delta\cos\gamma & -\sin\delta\sin\gamma & \cos\delta \end{bmatrix} \underline{v}_g. \tag{A1}$$

The inverse transformation is simply given by the matrix transpose.

Using Eq. (A1), the components of the ambient velocity vector $\boldsymbol{u}_\infty$ in the nacelle-attached frame are readily found to be $\underline{u}_{\infty n} = u_\infty\{\cos\delta\cos\gamma, \sin\delta, \sin\delta\cos\gamma\}^T$, where the scalar wind speed is $u_\infty = |\boldsymbol{u}_\infty|$, while $\underline{x}_{n_n} = \{1,0,0\}^T$. Hence, it follows that

$$\frac{\boldsymbol{u}_\infty}{u_\infty} \cdot \boldsymbol{x}_n = \cos\mu = \cos\delta\cos\gamma. \tag{A2}$$

A2 Transformation from wake-deflection to ground frame of reference

The nacelle and wake-deflection frames share the same unit vector $\boldsymbol{x}_n = \boldsymbol{x}_d$, which corresponds to the rotor axis of rotation. The $\boldsymbol{z}_d$ unit vector is orthogonal to the plane composed by $\boldsymbol{u}_\infty$ and $\boldsymbol{x}_d$, and therefore it can be written as $\boldsymbol{z}_d = z\boldsymbol{x}_d \times \boldsymbol{u}_\infty$, where z is a normalization scalar such that $\boldsymbol{z}\cdot\boldsymbol{z} = 1$. Performing the cross product and the normalization, one finds $\underline{z}_{d_n} = z\{0, -\sin\delta\cos\gamma, \sin\gamma\}^T$ and $z = 1/\sqrt{\cos^2\gamma\sin^2\delta + \sin^2\gamma} = 1/\sin\mu$. A right-handed triad is completed by setting $\boldsymbol{y}_d = -\boldsymbol{x}_d \times \boldsymbol{z}_d$, which yields $\underline{y}_{d_n} = z\{0, \sin\gamma, \sin\delta\cos\gamma\}^T$. The transformation matrix between the wake-deflection and nacelle-fixed components is therefore readily obtained as

$$\underline{v}_n = \begin{bmatrix} 1 & 0 & 0 \\ 0 & z\sin\gamma & -z\sin\delta\cos\gamma \\ 0 & z\sin\delta\cos\gamma & z\sin\gamma \end{bmatrix} \underline{v}_d. \tag{A3}$$

Finally, the transformation between wake-deflection and ground-fixed components follows by using Eq. (A3) and Eq. (A1), which yields

$$\underline{v}_g = \begin{bmatrix} \cos\delta\cos\gamma & \sin\gamma & \sin\delta\cos\gamma \\ -\cos\delta\sin\gamma & \cos\gamma & -\sin\delta\sin\gamma \\ -\sin\delta & 0 & \cos\delta \end{bmatrix} \begin{bmatrix} 1 & 0 & 0 \\ 0 & z\sin\gamma & -z\cos\gamma\sin\delta \\ 0 & z\cos\gamma\sin\delta & z\sin\gamma \end{bmatrix} \underline{v}_d, \tag{A4a}$$

$$= \begin{bmatrix} \cos\delta\cos\gamma & 1/z & 0 \\ -\cos\delta\sin\gamma & z\cos^2\delta\sin\gamma\cos\gamma & -z\sin\delta \\ -\sin\delta & z\sin\delta\cos\delta\cos\gamma & z\cos\delta\sin\gamma \end{bmatrix} \underline{v}_d. \tag{A4b}$$

The inverse transformation is simply given by the matrix transpose.

Using Eq. (A4b), the longitudinal (given by Eq. 11) and lateral (sidewash, given by Eq. 13) flow velocity components at the streamtube outlet can be transformed into the corresponding longitudinal and lateral components in the ground frame:

$$\frac{v_{o,g}}{u_\infty} = \frac{C_T}{4}\cos\delta\sin\gamma, \tag{A5a}$$

https://doi.org/10.5194/wes-2023-133
Preprint. Discussion started: 6 November 2023

$$\frac{w_{o,g}}{u_\infty} = \frac{C_T}{4}\sin\delta. \tag{A5b}$$

Appendix B: Experimental data set

Figures B1 and B2 report the blade pitch θ_p and tip speed ratio λ measured in the wind tunnel experiments.

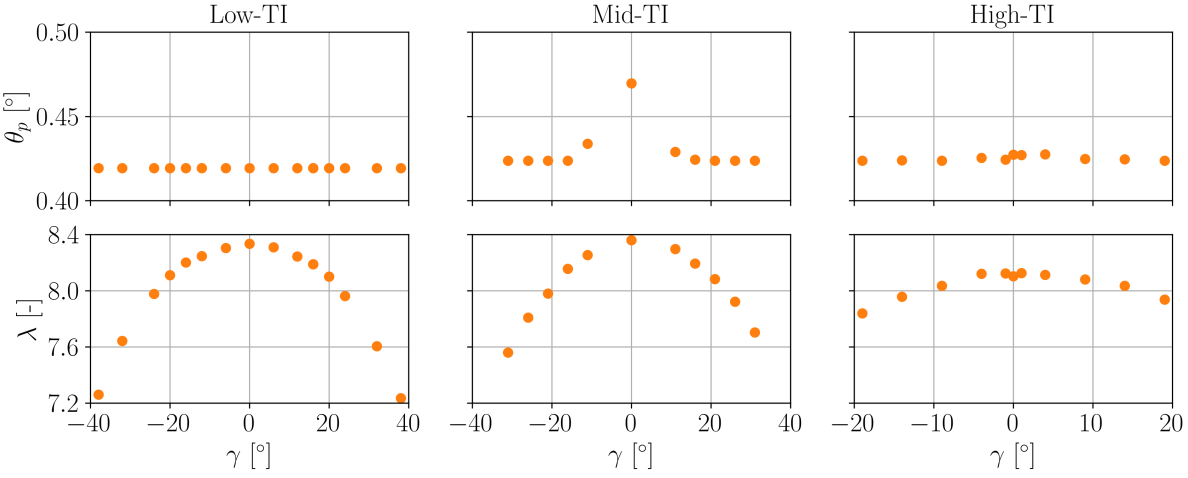

Figure B1. Average blade pitch angle θ_p (top row) and tip speed ratio λ (bottom row), for the full-power case in the three inflow cases Low-TI, Mid-TI, and High-TI.

https://doi.org/10.5194/wes-2023-133
Preprint. Discussion started: 6 November 2023

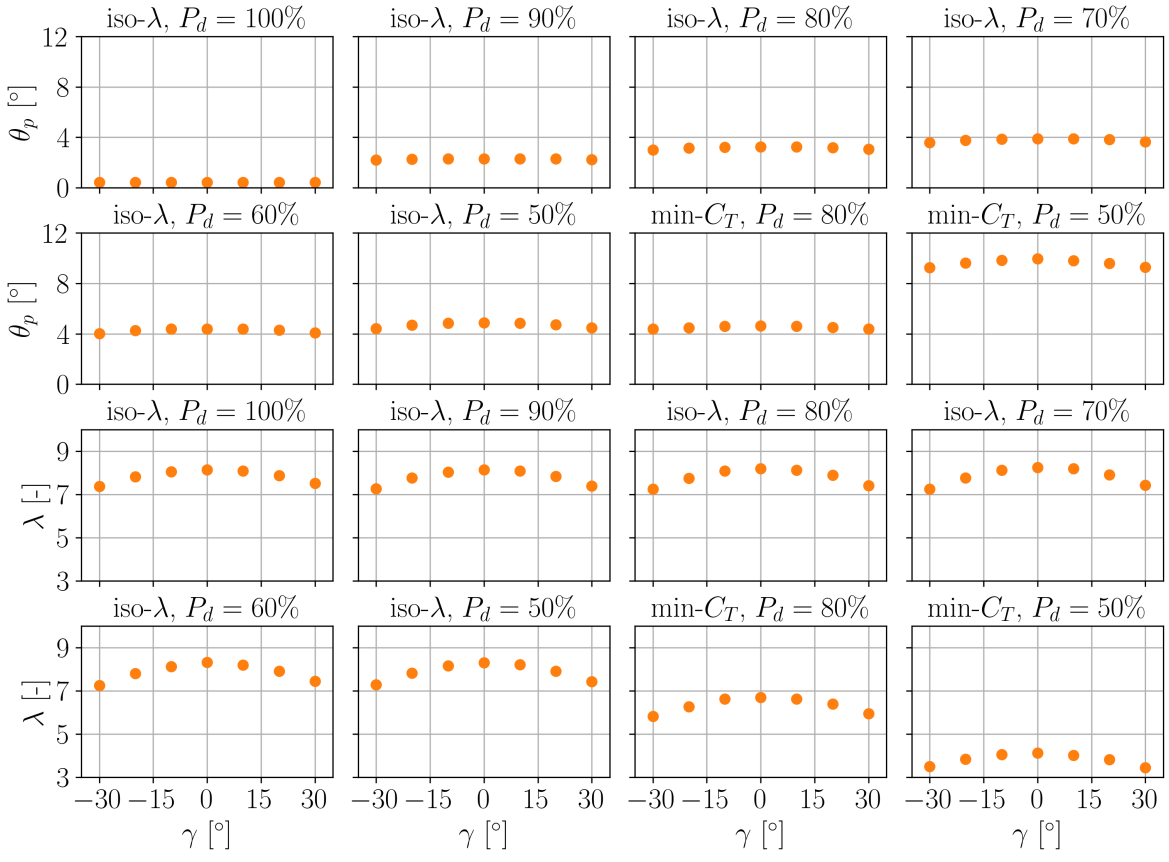

Figure B2. Average blade pitch angle θ_p (two top rows) and tip speed ratio λ (two bottom rows), for the derating cases in the Mid-TI inflow.

https://doi.org/10.5194/wes-2023-133
Preprint. Discussion started: 6 November 2023

eawe european academy of wind energy
Open Access WIND ENERGY SCIENCE DISCUSSIONS

Appendix C: Nomenclature

A	Area
a	Axial induction
B	Number of blades
C_D	Drag coefficient
C_L	Lift coefficient
$C_{L,\alpha}$	Lift slope
C_P	Power coefficient
C_T	Thrust coefficient
D	Rotor diameter
F_n	Normal force
F_t	Tangential force
k	Linear vertical wind shear coefficient
$\dot{m}$	Mass flux
p	Pressure
P	Power
P_d	Power demand (derating)
Q	Rotor torque
R	Rotor radius
r	Spanwise coordinate
T	Thrust force
u_∞	Free-stream wind speed
$u_{\infty,\text{hub}}$	Free-stream wind speed at hub height
u	Longitudinal velocity component
u_n	Rotor-orthogonal velocity component
u_t	Rotor-tangential velocity component
v	Lateral velocity component
x	Cartesian coordinate
y	Cartesian coordinate
z	Cartesian coordinate
α	Angle of attack
β	Blade twist angle
δ	Rotor tilt angle

https://doi.org/10.5194/wes-2023-133
Preprint. Discussion started: 6 November 2023

eawe european academy of wind energy
Open Access WIND ENERGY SCIENCE DISCUSSIONS

η_P	Power loss factor
η_T	Thrust change factor
γ	Rotor yaw angle
λ	Tip speed ratio
μ	Rotor total (true) misalignment angle
Ω	Rotor angular speed
φ	Inflow angle
Φ	Wind direction
ψ	Rotor azimuth angle
ρ	Air density
θ	Local pitch angle
θ_p	Blade pitch angle

$\underline{v}_f$	Components of vector $\boldsymbol{v}$ in frame f
$(\cdot)_g$	Quantity evaluated in the ground frame of reference
$(\cdot)_r$	Quantity evaluated in the nacelle frame of reference
$(\cdot)_d$	Quantity evaluated in the wake-deflection intrinsic frame of reference
$(\cdot)_{1s}$	Once-per-revolution sine harmonic
$(\cdot)_{1c}$	Once-per-revolution cosine harmonic

0P	Zeroth (constant) harmonic
1P	One per revolution harmonic
ALM	Actuator Line Method
BEM	Blade Element Momentum
CFD	Computational Fluid Dynamics
CTA	Constant Temperature Anemometry
FLORIS	FLOw Redirection and Induction in Steady State
LES	Large Eddy Simulation
RPM	Revolutions Per Minute
SOWFA	Simulator fOr Wind Farm Applications
TI	Turbulence Intensity

https://doi.org/10.5194/wes-2023-133
Preprint. Discussion started: 6 November 2023

eawe european academy of wind energy
Open Access WIND ENERGY SCIENCE DISCUSSIONS

Code and data availability. An implementation of the model described in this article in the FLORIS framework is available on Github at https://doi.org/10.5281/zenodo.8388901 (Tamaro et al., 2023). The repository also contains all the data and the Jupyter notebooks used to generate the figures. The code and the scripts to reproduce the figures can be run on Binder at the link https://tinyurl.com/btcl-main. The notebook of Fig. 5 can be used to interactively plot the thrust and power coefficients for other user-defined values of the model parameters. The notebooks of Figs. 14 and 15 contain also the code used for computing the optimal control policies.

Author contributions. CLB developed the formulation of the misalignment model, and supervised the overall research. ST implemented the model, performed the LES simulations and the corresponding model validation, and conducted the wake-steering analyses with FLORIS. FC performed the validation with respect to the experimental measurements. All authors contributed to the interpretation of the results. CLB and ST wrote the manuscript, with contributions by FC in the experimental section. All authors provided important input to this research work through discussions and feedback and by improving the manuscript.

Competing interests. The authors declare that they have no conflict of interest, except for CLB who is the Editor in Chief of the Wind Energy Science journal.

Financial support. This work has been supported in part by the PowerTracker project, which receives funding from the German Federal Ministry for Economic Affairs and Climate Action (FKZ: 03EE2036A). This work has also been partially supported by the MERIDIONAL project, which receives funding from the European Union's Horizon Europe Programme under the grant agreement No. 101084216.

Acknowledgements. The authors express their gratitude to the Leibniz Supercomputing Centre (LRZ) for providing access and computing time on the SuperMUC Petascale System under Projekt-ID pr84be "Large-eddy Simulation for Wind Farm Control".

https://doi.org/10.5194/wes-2023-133
Preprint. Discussion started: 6 November 2023

eawe european academy of wind energy
Open Access WIND ENERGY SCIENCE DISCUSSIONS

References

Abramowitz, M., Stegun, I. A., and Romer, R. H.: Handbook of Mathematical Functions with Formulas, Graphs, and Mathematical Tables, American Journal of Physics, 56, 958–958, https://doi.org/10.1119/1.15378, 1988.

Baratron: Baratron, https://www.mks.com/, 2022.

Bartl, J., Mühle, F., Schottler, J., Sætran, L., Peinke, J., Adaramola, M., and Hölling, M.: Wind tunnel experiments on wind turbine wakes in yaw: effects of inflow turbulence and shear, Wind Energy Science, 3, 329–343, https://doi.org/10.5194/wes-3-329-2018, 2018.

Bortolotti, P., Tarres, H. C., Dykes, K. L., Merz, K., Sethuraman, L., Verelst, D., and Zahle, F.: IEA Wind TCP Task 37: Systems Engineering in Wind Energy - WP2.1 Reference Wind Turbines, Tech. rep., National Renewable Energy Lab. (NREL), https://doi.org/10.2172/1529216, 2019.

Bottasso, C. L. and Campagnolo, F.: Wind Tunnel Testing of Wind Turbines and Farms, in: Handbook of Wind Energy Aerodynamics, edited by Stoevesandt, B., Schepers, G., Fuglsang, P., and Sun, Y., pp. 1077–1126, Springer International Publishing, Cham, https://doi.org/10.1007/978-3-030-31307-4_54, 2022a.

Bottasso, C. L. and Campagnolo, F.: Wind tunnel testing of wind turbines and farms, Handbook of Wind Energy Aerodynamics, pp. 1077–1126, 2022b.

Bottasso, C. L., Campagnolo, F., and Petrović, V.: Wind tunnel testing of scaled wind turbine models: Beyond aerodynamics, J. Wind Eng. Ind. Aerodyn, 127, 2014.

Campagnolo, F., Petrović, V., Schreiber, J., Nanos, E. M., Croce, A., and Bottasso, C. L.: Wind tunnel testing of a closed-loop wake deflection controller for wind farm power maximization, Journal of Physics: Conference Series, 753, 032 006, https://doi.org/10.1088/1742-6596/753/3/032006, 2016.

Campagnolo, F., Weber, R., Schreiber, J., and Bottasso, C. L.: Wind tunnel testing of wake steering with dynamic wind direction changes, Wind Energy Science, 5, 1273–1295, https://doi.org/10.5194/wes-5-1273-2020, 2020a.

Campagnolo, F., Weber, R., Schreiber, J., and Bottasso, C. L.: Wind tunnel testing of wake steering with dynamic wind direction changes, Wind Energy Science, 5, 1273–1295, https://doi.org/10.5194/wes-5-1273-2020, 2020b.

Campagnolo, F., Tamaro, S., Mühle, F., and Bottasso, C. L.: Wind Tunnel testing of Combined Derating and Wake Steering by Yawing, in: IFAC World Congress 2023, International federation of Automatic Control, Yokohama, JAPAN, under review, 2023.

Coleman, R. P., Feingold, A. M., and Stempin, C. W.: Evaluation of the Induced-Velocity Field of an Idealized Helicopter Rotor, Wartime report, National Advisory Committee for Aeronautics, Langley Memorial Aeronautical Laboratory, 1945.

Cossu, C.: Wake redirection at higher axial induction, Wind Energy Science, 6, 377–388, https://doi.org/10.5194/wes-6-377-2021, 2021a.

Cossu, C.: Evaluation of tilt control for wind-turbine arrays in the atmospheric boundary layer, Wind Energy Science, 6, 663–675, https://doi.org/10.5194/wes-6-663-2021, 2021b.

Dahlberg, J. and Montgomerie, B.: Research program of the utgrunden demonstration offshore wind farm, final report part 2, wake effects and other loads, Technical report 02-17, Swedish Defense Research Agency (FOI), Kista, Sweden, 2005.

Doekemeijer, B. M., Kern, S., Maturu, S., Kanev, S., Salbert, B., Schreiber, J., Campagnolo, F., Bottasso, C. L., Schuler, S., Wilts, F., Neumann, T., Potenza, G., Calabretta, F., Fioretti, F., and van Wingerden, J.-W.: Field experiment for open-loop yaw-based wake steering at a commercial onshore wind farm in Italy, Wind Energy Science, 6, 159–176, https://doi.org/10.5194/wes-6-159-2021, 2021.

https://doi.org/10.5194/wes-2023-133
Preprint. Discussion started: 6 November 2023

Draper, M., Guggeri, A., López, B., Díaz, A., Campagnolo, F., and Usera, G.: A Large Eddy Simulation framework to assess wind farm power maximization strategies: Validation of maximization by yawing, Journal of Physics: Conference Series, 1037, 072 051, https://doi.org/10.1088/1742-6596/1037/7/072051, 2018.

Fleming, P., Gebraad, P. M., Lee, S., van Wingerden, J.-W., Johnson, K., Churchfield, M., Michalakes, J., Spalart, P., and Moriarty, P.: Simulation comparison of wake mitigation control strategies for a two-turbine case, Wind Energy, 18, 2135–2143, https://doi.org/https://doi.org/10.1002/we.1810, 2015.

Fleming, P., Annoni, J., Shah, J. J., Wang, L., Ananthan, S., Zhang, Z., Hutchings, K., Wang, P., Chen, W., and Chen, L.: Field test of wake steering at an offshore wind farm, Wind Energy Science, 2, 229–239, https://doi.org/10.5194/wes-2-229-2017, 2017.

Fleming, P., Annoni, J., Churchfield, M., Martinez-Tossas, L. A., Gruchalla, K., Lawson, M., and Moriarty, P.: A simulation study demonstrating the importance of large-scale trailing vortices in wake steering, Wind Energy Science, 3, 243–255, https://doi.org/10.5194/wes-3-243-2018, 2018.

Fleming, P., King, J., Dykes, K., Simley, E., Roadman, J., Scholbrock, A., Murphy, P., Lundquist, J. K., Moriarty, P., Fleming, K., van Dam, J., Bay, C., Mudafort, R., Lopez, H., Skopek, J., Scott, M., Ryan, B., Guernsey, C., and Brake, D.: Initial results from a field campaign of wake steering applied at a commercial wind farm – Part 1, Wind Energy Science, 4, 273–285, https://doi.org/10.5194/wes-4-273-2019, 2019.

Fleming, P. A., Gebraad, P. M., Lee, S., van Wingerden, J.-W., Johnson, K., Churchfield, M., Michalakes, J., Spalart, P., and Moriarty, P.: Evaluating techniques for redirecting turbine wakes using SOWFA, Renewable Energy, 70, 211–218, https://doi.org/https://doi.org/10.1016/j.renene.2014.02.015, special issue on aerodynamics of offshore wind energy systems and wakes, 2014.

Forsting, A. M., van der Laan, M., and Troldborg, N.: The induction zone/factor and sheared inflow: A linear connection?, Journal of Physics: Conference Series, 1037, 072 031, https://doi.org/10.1088/1742-6596/1037/7/072031, 2018.

Gao, F. and Han, L.: Implementing the Nelder-Mead simplex algorithm with adaptive parameters, Computational Optimization and Applications, 51, 259–277, https://doi.org/10.1007/s10589-010-9329-3, 2012.

Gebraad, P. M. O., Teeuwisse, F. W., van Wingerden, J. W., Fleming, P. A., Ruben, S. D., Marden, J. R., and Pao, L. Y.: Wind plant power optimization through yaw control using a parametric model for wake effects—a CFD simulation study, Wind Energy, 19, 95–114, https://doi.org/https://doi.org/10.1002/we.1822, 2016.

Hansen, M.: Aerodynamics of wind turbines: Third edition, Routledge, https://doi.org/10.4324/9781315769981, 2015.

Heck, K. S., Johlas, H. M., and Howland, M. F.: Modeling the induction, thrust, and power of a yaw misaligned actuator disk, https://doi.org/10.48550/ARXIV.2209.00111, 2022.

Howland, M. F., Gonzalez, C. M., Martinez, J. J. P., Quesada, J. B., Larranaga, F. P., Yadav, N. K., Chawla, J. S., and Dabiri, J. O.: Influence of atmospheric conditions on the power production of utility-scale wind turbines in yaw misalignment, https://doi.org/10.48550/ARXIV.2008.00873, 2020.

Hulsman, P., Sucameli, C., Petrović, V., Rott, A., Gerds, A., and Kühn, M.: Turbine power loss during yaw-misaligned free field tests at different atmospheric conditions, Journal of Physics: Conference Series, 2265, 032 074, https://doi.org/10.1088/1742-6596/2265/3/032074, 2022.

Jiménez, A., Crespo, A., and Migoya, E.: Application of a LES technique to characterize the wake deflection of a wind turbine in yaw, Wind Energy, 13, 559–572, https://doi.org/https://doi.org/10.1002/we.380, 2010.

Johnson, W.: Helicopter Theory, Dover Books on Aeronautical Engineering, Dover Publications, 1995.

https://doi.org/10.5194/wes-2023-133
Preprint. Discussion started: 6 November 2023

Jonkman, J., Butterfield, S., Musial, W., and Scott, G.: Definition of a 5-MW Reference Wind Turbine for Offshore System Development, Tech. rep., National Renewable Energy Laboratory, https://doi.org/10.2172/947422, 2009.

Juangarcia, D. A., Eguinoa, I., and Knudsen, T.: Derating a single wind farm turbine for reducing its wake and fatigue, Journal of Physics: Conference Series, 1037, 032 039, https://doi.org/10.1088/1742-6596/1037/3/032039, 2018.

Katz, J. and Plotkin, A.: Low-Speed Aerodynamics, Cambridge Aerospace Series, Cambridge University Press, 2 edn., https://doi.org/10.1017/CBO9780511810329, 2001.

King, J., Fleming, P., King, R., Martínez-Tossas, L. A., Bay, C. J., Mudafort, R., and Simley, E.: Control-oriented model for secondary effects of wake steering, Wind Energy Science, 6, 701–714, https://doi.org/10.5194/wes-6-701-2021, 2021.

Krogstad, P.-A. and Adaramola, M. S.: Performance and near wake measurements of a model horizontal axis wind turbine, Wind Energy, 15, 743–756, https://doi.org/https://doi.org/10.1002/we.502, 2012.

Liew, J., Urbán, A. M., and Andersen, S. J.: Analytical model for the power–yaw sensitivity of wind turbines operating in full wake, Wind Energy Science, 5, 427–437, https://doi.org/10.5194/wes-5-427-2020, 2020.

Martínez-Tossas, L. A., King, J., Quon, E., Bay, C. J., Mudafort, R., Hamilton, N., Howland, M. F., and Fleming, P. A.: The curled wake model: a three-dimensional and extremely fast steady-state wake solver for wind plant flows, Wind Energy Science, 6, 555–570, https://doi.org/10.5194/wes-6-555-2021, 2021.

Martínez-Tossas, L. A. and Meneveau, C.: Filtered lifting line theory and application to the actuator line model, Journal of Fluid Mechanics, 863, 269–292, https://doi.org/10.1017/jfm.2018.994, 2019.

Medici, D.: Experimental studies of wind turbine wakes : power optimisation and meandering, Ph.D. thesis, Royal Institute of Technology, Stockholm, Sweden, 2005.

Meyers, J., Bottasso, C. L., Dykes, K., Fleming, P., Gebraad, P., Giebel, G., Göçmen, T., and van Wingerden, J.-W.: Wind Farm Flow Control: Prospects and Challenges, Wind Energy Science Discussions, https://doi.org/https://doi.org/10.5194/wes-2022-24, 2022.

Nanos, E. M., Bottasso, C. L., Tamaro, S., Manolas, D. I., and Riziotis, V. A.: Vertical wake deflection for floating wind turbines by differential ballast control, Wind Energy Science, 7, 1641–1660, https://doi.org/10.5194/wes-7-1641-2022, 2022.

NREL: AeroDyn Users Guide and Theory Manual, https://github.com/OpenFAST/OpenFAST/blob/main/docs/source/user/aerodyn/index.rst, accessed 19 March 2023, 2023a.

NREL: FLORIS, Version 3, https://github.com/NREL/floris, accessed 19 March 2023, 2023b.

NREL: OpenFAST, https://github.com/openfast, accessed 19 March 2023, 2023c.

Pedersen, M. M., van der Laan, P., Friis-Møller, M., Rinker, J., and Réthoré, P.-E.: DTUWindEnergy/PyWake: PyWake, https://doi.org/10.5281/zenodo.2562662, 2019.

Pitt, D. M. and Peters, D. A.: Theoretical prediction of dynamic inflow derivatives, Vertica, 5, 1981.

Schottler, J., Hölling, A., Peinke, J., and Hölling, M.: Brief communication: On the influence of vertical wind shear on the combined power output of two model wind turbines in yaw, Wind Energy Science, 2, 439–442, https://doi.org/10.5194/wes-2-439-2017, 2017.

Simley, E., Fleming, P., Girard, N., Alloin, L., Godefroy, E., and Duc, T.: Results from a wake-steering experiment at a commercial wind plant: investigating the wind speed dependence of wake-steering performance, Wind Energy Science, 6, 1427–1453, https://doi.org/10.5194/wes-6-1427-2021, 2021.

Tamaro, S., Campagnolo, F., and Bottasso, C. L.: On the power and control of a misaligned rotor – Beyond the cosine law –, Zenodo [source code and data set], https://doi.org/10.5281/zenodo.8378703, 2023.

https://doi.org/10.5194/wes-2023-133
Preprint. Discussion started: 6 November 2023

Tietjens, O. and Prandtl, L.: Applied Hydro- and Aeromechanics: Based on Lectures of L. Prandtl, no. Bd. 2 in Applied hydro- and aeromechanics: based on lectures of L. Prandtl, Dover Publications, https://books.google.de/books?id=Ds-bd0zAwIYC, 1957.

Troldborg, N., Sørensen, J. N., and Mikkelsen, R.: Actuator Line Simulation of Wake of Wind Turbine Operating in Turbulent Inflow, Journal of Physics: Conference Series, 75, 012 063, https://doi.org/10.1088/1742-6596/75/1/012063, 2007.

Wang, C., Wang, J., Campagnolo, F., Carraón, D. B., and Bottasso, C. L.: Validation of large-eddy simulation of scaled waked wind turbines in different yaw misalignment conditions, Journal of Physics: Conference Series, 1037, 062 007, https://doi.org/10.1088/1742-6596/1037/6/062007, 2018.

Wang, C., Campagnolo, F., and Bottasso, C. L.: Identification of airfoil polars from uncertain experimental measurements, Wind Energy Science, 5, 1537–1550, https://doi.org/10.5194/wes-5-1537-2020, 2020.

Wang, C., Campagnolo, F., Canet, H., Barreiro, D. J., and Bottasso, C. L.: How realistic are the wakes of scaled wind turbine models?, Wind Energy Science, 6, 961–981, https://doi.org/10.5194/wes-6-961-2021, 2021.

Wang, J., Wang, C., Campagnolo, F., and Bottasso, C. L.: Wake behavior and control: comparison of LES simulations and wind tunnel measurements, Wind Energy Science, 4, 71–88, https://doi.org/10.5194/wes-4-71-2019, 2019.